Solar Phys (2011) 273:309–337
DOI 10.1007/s11207-011-9788-4



# Radio Emission of the Quiet Sun and Active Regions (Invited Review)

**K. Shibasaki · C.E. Alissandrakis · S. Pohjolainen**

Received: 9 February 2011 / Accepted: 8 May 2011 / Published online: 15 June 2011


**Abstract** Solar radio emission provides valuable information on the structure and dynamics of the solar atmosphere above the temperature minimum. We review the background and most recent observational and theoretical results on the quiet Sun and active region studies, covering the entire radio range from millimeter to decameter wavelengths. We examine small- and large-scale structures, at short and long time scales, as well as synoptic aspects. Open questions and challenges for the future are also identified.

**Keywords** Chromosphere, quiet · Corona, quiet · Polarization, radio · Radio emission, quiet · Active regions, radio

## 1. Introduction

Solar radio emission is traditionally divided into a background component (quiet sun, QS), a slowly varying component (associated mainly with active regions), and a sporadic (burst) component (Kundu, 1965). Both short- and long-lived transient emissions can occur in quiet regions, thus the 'quiet' emission may not be that quiet after all – it can be intense and show considerable time variation.

Energy Storage and Release through the Solar Activity Cycle – Models Meet Radio Observations
Guest Editors: Christophe Marqué and Alexander Nindos

K. Shibasaki
Nobeyama Solar Radio Observatory/NAOJ, Nagano 384-1305, Japan
e-mail: shibasaki@nro.nao.ac.jp

C.E. Alissandrakis
Section of Astro-Geophysics, Department of Physics, University of Ioannina, 45110 Ioannina, Greece
e-mail: calissan@cc.uoi.gr

S. Pohjolainen (✉)
Department of Physics and Astronomy, Tuorla Observatory, University of Turku, 21500 Piikkiö, Finland
e-mail: silpoh@utu.fi

Compared to the other components of the solar radio emission, as well as to quiet emission in other spectral ranges (*e.g.*, the EUV), the radio quiet Sun has the advantage of being fairly well understood as originating from thermal bremsstrahlung in local thermodynamic equilibrium (LTE). It can thus be used as a powerful diagnostic of the physical conditions in a wide range of atmospheric layers. As the opacity increases with the wavelength of observation, the effective height of formation moves from the temperature minimum (at sub-millimeter waves) to the low corona (at meter waves), or even higher into the corona and the heliosphere (longer wavelengths being observed from space).

In the metric range, in addition to opacity effects, we have to consider refraction and total reflection. The latter makes solar radio emission a useful tool in determining source heights; radio waves from a particular atmospheric layer will reach the observer only if their frequency is higher than the local plasma frequency. As the electron density decreases with height, so does the critical plasma frequency. Thus, both opacity and refraction contribute so that we can form a 3D-view of the solar atmosphere from multi-wavelength observations.

In this review we describe how our understanding of the quiet Sun has evolved over the years and give emphasis on recent results on the quiet Sun phenomena, based on radio observations and comparisons to other wavelength data. For reviews on earlier work see, *e.g.*, Alissandrakis (1994), Gary (1996), Alissandrakis and Einaudi (1997), Lantos (1999), Shibasaki (1999), and Keller and Krucker (2004).

In Section 2 we discuss the formation of radiation and the radio spectrum, in Section 3 we give an overview of high-resolution radio imaging observations, and in Section 4 we describe the quiet Sun features that have been studied extensively using radio observations. In Section 5 we discuss briefly the active region emission, in order to present a complete picture of the non-flaring Sun. The last section is devoted to future challenges in radio studies of the quiet Sun, where we discuss the present and future radio instrumentation, questions on data analysis, and the current theoretical issues.

## 2. Radiative Transfer and Modeling

### 2.1. The Basics

The quiet Sun emission at radio wavelengths is the simplest case for modeling for a number of reasons. The radiation is of thermal origin, from the ambient plasma; the mechanism is bremsstrahlung (free–free) from electrons interacting with ions in the presence of a relatively weak magnetic field. The magnetic field is weak enough so that gyro-resonance emission can safely be ignored; since the opacity at the 4th and higher harmonics layers is negligible, the condition is that the observing frequency should be higher than three times the local gyrofrequency, which gives $B$ (in G) $< f$ (in MHz)/8.4, *i.e.* 3600 G at 1 cm and 36 G at 1 m.

The electrons are always in LTE, and thus one can assume that the source function is equal to the Planck function. Moreover, thanks to the Rayleigh–Jeans approximation, it is convenient to express the specific intensity of radiation in terms of brightness temperature, $T_\mathrm{b}$, and the Planck function in terms of electron temperature $T_\mathrm{e}$. Thus, the solution of the transfer equation in a magnetoionic medium takes the form

$$T_{\mathrm{b},j} = \int_0^\infty T_\mathrm{e}(\tau_j) e^{-\tau_j}\, \mathrm{d}\tau_j, \tag{1}$$

where $j = 1$ for the extraordinary mode and $j = 2$ for the ordinary mode, $T_e(\tau_j)$ is the distribution of the electron temperature along the line of sight, and $\tau_j$ is the optical depth, related to the path $\ell$ along the line of sight through

$$d\tau_j = -k_j(T_e, N_e)\, d\ell, \tag{2}$$

where $T_e(\ell)$ and $N_e(\ell)$ represent the variations of electron temperature and density along the line of sight. In the case of a plane-parallel atmosphere, $\ell$ and $\tau_j$ in Equations (1) and (2) can be replaced by $\ell/\mu$ and $\tau_j/\mu$, respectively, where $\mu = \cos\theta$, $\theta$ being the angle between the direction of the line of sight and the direction of the center of the solar disk.

The free–free absorption coefficient at frequency $f$ has the well-known form (Kundu, 1965)

$$k_j(T_e, N_e) = \xi \frac{N_e^2}{n_j f^2 T_e^{3/2}} A_j(B, \theta), \tag{3}$$

where $\xi$ is a slowly varying function of $T_e$ and $N_e$, $n_j$ the index of refraction ($\sim$1 at short wavelengths) and $A_j(B, \theta)$ is a function of the magnitude of the magnetic field $B$ and its angle with the line of sight, $\theta$ (Zheleznyakov, 1970).

In the absence of magnetic field, $A_j = 1$. Otherwise the extraordinary mode opacity is slightly above that of the unmagnetized case, whereas the ordinary opacity is below; since in the region of formation of radiation the temperature increases with height, the same thing happens to the brightness temperature. The net effect is weakly polarized emission in the sense of the extraordinary mode, which is a powerful diagnostic of the magnetic field (see, *e.g.*, Grebinskij *et al.*, 2000). We should note that, far from the center of the disk, the observed circular polarization is influenced by propagation effects (Cohen, 1960), which are stronger at longer wavelengths. Thus, the circular polarization is sometimes more useful as a diagnostic of the magnetic field in the propagation region, rather than as a diagnostic of the physical conditions at the source (Alissandrakis, 1999; Ryabov *et al.*, 1999)

It follows from the above that all we need to know in order to compute the total intensity $I = \frac{1}{2}(T_{b,1} + T_{b,2})$, and the circular polarization $V = \frac{1}{2}(T_{b,1} - T_{b,2})$ of the radiation, is $T_e(\ell)$, $N_e(\ell)$, and, if applicable, $B(\ell)$, and $\theta(\ell)$. There is no need to consider non-LTE effects, abundances, ionization and excitation equilibria that are common sources of uncertainty in other parts of the spectrum.

Things are not always that simple though. One inconvenience is the large radial extent of the region of formation of radiation at cm-waves, as the chromosphere–corona transition region (TR) is too thin to provide any sizable opacity. This makes it difficult to define the effective height of formation.

Complications also arise at longer wavelengths, where the index of refraction departs from unity. This does not only affect the ray paths, but also decreases the brightness, as the rays divert away from high density regions and the total optical depth drops below unity (*cf.* Figure 1 of Alissandrakis, 1994). Scattering of the radiation in inhomogeneities can have similar effects (see Thejappa and MacDowall, 2008 and earlier works by Aubier, Leblanc, and Boischot, 1971; Hoang and Steinberg, 1977; Thejappa and Kundu, 1992; 1994; Bastian, 1994). Scattering also smoothes structures of small angular scale and increases the apparent size of the radio Sun.

### 2.2. One-Dimensional Models of the Radio Spectrum

Anyone who has seen a solar image will agree that the Sun is rich in fine structures. As a matter of fact, inhomogeneities become more important as we move from the photosphere to

the corona. Under these circumstances, it is rather surprising that one-dimensional models, which treat the physical parameters as a function of height only and assume hydrostatic equilibrium, have any resemblance to the observations at all. The physical reason behind their success is the strong radial stratification of the solar atmosphere, due to gravity. Besides the average QS, coronal holes are another favorite for one-dimensional models, as we will discuss in Section 4.5.

There is a long tradition of empirical solar models. The Bilderberg Continuum Atmosphere (BCA; Gingerich and de Jager, 1968), which superseded the Utrecht Reference Photosphere (URP; Heintze, Hubenet, and de Jager, 1964), was the first to take into account mm-wave observations together with EUV; a comparison between BCA-predicted brightness temperatures and observations in the range of 0.0086 – 15.8 mm was presented in Noyes, Beckers, and Low (1968), in their Figure 7. The Harvard Smithsonian Reference Atmosphere (HSRA; Gingerich *et al.*, 1971) followed, and the brightness computations and comparison with data were extended to 10 cm (their Figure 3).

However, these models did not extend beyond the low chromosphere; they all stopped around $T_e \simeq 10^4$ K, which is too low for model computations at longer wavelengths. The VAL models that followed (Vernazza, Avrett, and Loeser, 1973, 1976, 1981) extended the temperature range up to $3\times10^4$ K, into the lower part of the transition region. The subsequent FAL models (Fontenla, Avrett, and Loeser, 1990, 1991, 1993) went up to $10^5$ K, while the model of Fontenla, Avrett, and Loeser (2002) reached the low corona at $1.2\times10^6$ K. These models also developed further the multi-component approach, first introduced by Vernazza, Avrett, and Loeser (1981), to represent different quiet and active regions on the Sun.

In the more recent models, by Fontenla *et al.* (2006), Fontenla, Balasubramaniam, and Harder (2007), and Fontenla *et al.* (2009), the emphasis has shifted again to the lower atmospheric layers (up to $10^4$ K). Still, Avrett and Loeser (2008) produced a model of the average quiet Sun chromosphere and TR up to $1.6\times10^6$ by extending model C (average quiet Sun) of Fontenla *et al.* (2006). The authors computed, among other things, the spectrum in the range of 0.04 – 40 mm. Their results are shown in Figure 1, together with the temperature *vs.* height variation of their model and the contribution functions at several wavelengths, including some in the short microwave range. Note that the microwave spectrum reproduces, as expected, the shape of the $T_e(z)$ curve. According to this figure, most of the emission at 3 cm and shorter wavelengths originates below the TR, with a small contribution from the latter and no contribution from the corona.

Figure 1 also shows the computations of Loukitcheva *et al.* (2004). They tried a number of static FAL models from Fontenla, Avrett, and Loeser (1993), and also made computations on the basis of the dynamic simulations of Carlsson and Stein (2002). Their conclusion was that the dynamic picture of the solar internetwork chromosphere is consistent with the currently available mm- and sub-mm brightness observations.

In order to compute brightness spectra at longer wavelengths, one has to add a coronal contribution. Zirin, Baumert, and Hurford (1991) found that their measurements, which extended up to 21 cm, could simply be reproduced by a two-component model: an optically thick chromosphere and an isothermal corona. We know, however, that there is a TR between these two. In a recent work, Selhorst, Silva, and Costa (2005) used a hybrid model (combination of models for the photosphere, chromosphere, and corona) to reproduce the observed features in Nobeyama Radioheliograph images at 17 GHz. To obtain acceptable brightness temperature values and the observed solar radius, they had to include absorbing chromospheric structures, such as spicules, into the model. Their computed spectrum is shown in Figure 2, together with a model by Bastian, Dulk, and Leblanc (1996) that covers approximately the same frequency range.

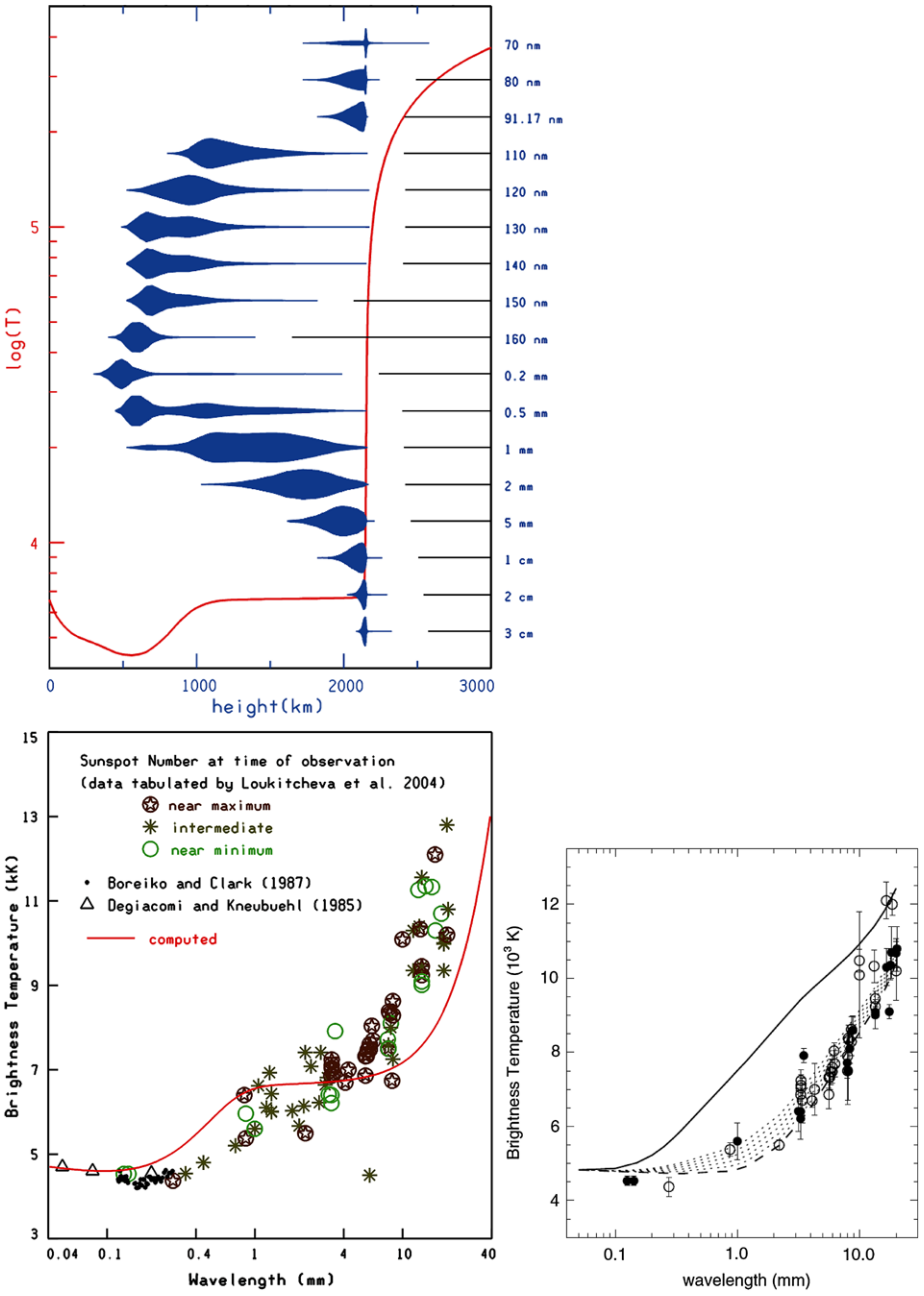


**Figure 1** Contribution functions at several wavelengths, including microwave, according to the model of Avrett and Loeser (2008) (top panel); the corresponding spectrum is shown in the bottom left panel. Reproduced by permission of the AAS. The bottom right panel shows spectra computed by Loukitcheva *et al.* (2004); solid line: on the basis of model F (network) of Fontenla, Avrett, and Loeser (1993); dashed line: on the basis of dynamic simulations by Carlsson and Stein (2002); dotted lines: combinations of the two. Reproduced with permission © ESO. Very similar results were obtained using model A (cell interior) of Fontenla, Avrett, and Loeser (1993), instead of the Carlsson and Stein model. Only data obtained near solar maximum and solar minimum are presented in this plot, as open and filled circles, respectively.

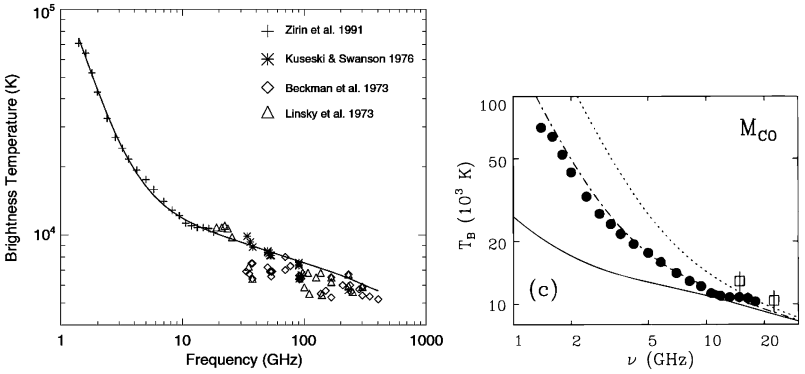


**Figure 2** Left: Observed brightness temperatures of the solar disk center (symbols) and the hybrid model fit (solid line) of Selhorst, Silva, and Costa (2005), presented over a wide frequency range. Reproduced with permission © ESO. Right: Spectra computed by Bastian, Dulk, and Leblanc (1996); solid line: on the basis of a model by Avrett (1995); dot-dashed line: with the addition of a minimum corona inferred by Zirin, Baumert, and Hurford (1991); dotted line: with the addition of three times the minimum corona. Filled circles are the measurements of Zirin, Baumert, and Hurford, squares are VLA measurements by Bastian, Dulk, and Leblanc. Reproduced by permission of the AAS.

The results presented in Figures 1 and 2 show that a model can be found that fits most microwave data, although there is a large scatter in the mm to sub-mm range due to inherent difficulties in the measurements and possible solar cycle effects. The main problem with these models is that the radio data are better fitted with models that represent the *cell interior*, rather than with average models, which predict too much radio flux.

All computations presented above start from standard atmospheric models. In a different approach, several authors have tried to use direct information from the EUV part of the spectrum to compute the radio brightness, which is reasonable since the radiation in both wavelength ranges is formed in the same atmospheric layers. In one approach the emission measure, EM, is used:

$$EM = \int_0^L N_e^2 \, d\ell \tag{4}$$

which appears in the expression for the intensity of EUV lines:

$$I = \frac{1}{4\pi} \int_0^L G(T_e, N_e) \, N_e^2 \, d\ell \simeq \frac{1}{4\pi} \langle G(T_e, N_e) \rangle \, EM, \tag{5}$$

where $G(T_e, N_e)$ is the contribution function for the line. The emission measure also appears in the expression for the radio brightness temperature; for an isothermal layer and negligible refraction we get from Equations (2) and (3):

$$\tau = \xi \frac{1}{f^2 T_e^{3/2}} \int_0^L N_e^2 \, d\ell = \xi \frac{EM}{f^2 T_e^{3/2}}. \tag{6}$$

Furthermore, if the layer is optically thin,

$$T_b \simeq \tau T_e = \xi \frac{EM}{f^2 T_e^{1/2}}. \tag{7}$$

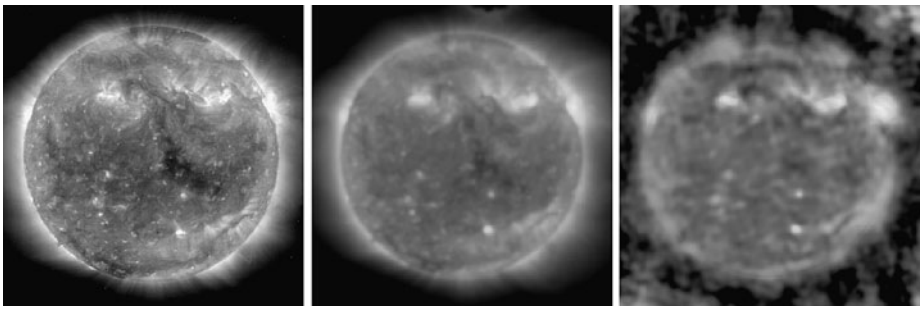

**Figure 3** EIT image at 195 Å (left), computed brightness (middle), and observed (VLA) brightness at 20 cm for November 11, 1997. Figure adapted from Zhang *et al.* (2001), reproduced by permission of the AAS.

It is a well-known practice to use two EUV lines for an estimate of the plasma temperature and the emission measure. Zhang *et al.* (2001) used three EIT images, at 171, 195 and 284 Å, to derive the emission measure in a two-temperature model. They used this information to compute the emission at 6 and 20 cm wavelengths, which they compared with their VLA observations. Figure 3 shows their results at 20 cm. Although the model image looks very much like the observed, the computed brightness temperature was twice the observed at both wavelengths. They attributed the discrepancy to errors in the coronal abundances used to infer the radio flux from the EIT data. Their results also raise the question of accuracy in temperature and emission measure computations from broad-band EUV images.

The differential emission measure (DEM) is even better than the emission measure; it is defined as

$$\varphi(T_\mathrm{e}) = N_\mathrm{e}^2 \frac{\mathrm{d}\ell}{\mathrm{d}T_\mathrm{e}} \tag{8}$$

and represents the distribution of electron density over a temperature range $T_1$ to $T_2$. Equations (5) and (6) are then replaced by

$$I = \frac{1}{4\pi} \int_{T_1}^{T_2} G(T_\mathrm{e}, N_\mathrm{e}) \varphi(T_\mathrm{e})\, \mathrm{d}T_\mathrm{e} \tag{9}$$

$$\tau = \frac{\xi}{f^2} \int_{T_1}^{T_2} T_\mathrm{e}^{-3/2} \varphi(T_\mathrm{e})\, \mathrm{d}T_\mathrm{e} \tag{10}$$

and the isothermal assumption is dropped. Obviously, one needs many EUV lines formed over the appropriate temperature range in order to make good use of the DEM.

Landi and Chiuderi Drago (2003) used the DEM values derived from UV and EUV spectral line intensities observed by SUMER and CDS, and showed that a TR model *for the cell interior* – excluding any network contribution – could give an agreement with the observed radio brightness temperatures. In a subsequent work Landi and Chiuderi Drago (2008) showed that radio observations provide a much more reliable diagnostic tool for the determination of the DEM than UV and EUV lines at $T < 30\,000$ K, since the latter are optically thick. Moreover, they extended the DEM down to 5600 K using the radio spectrum from 1.5 to 345 GHz, and obtained very good agreement with the radio data (Figure 4).

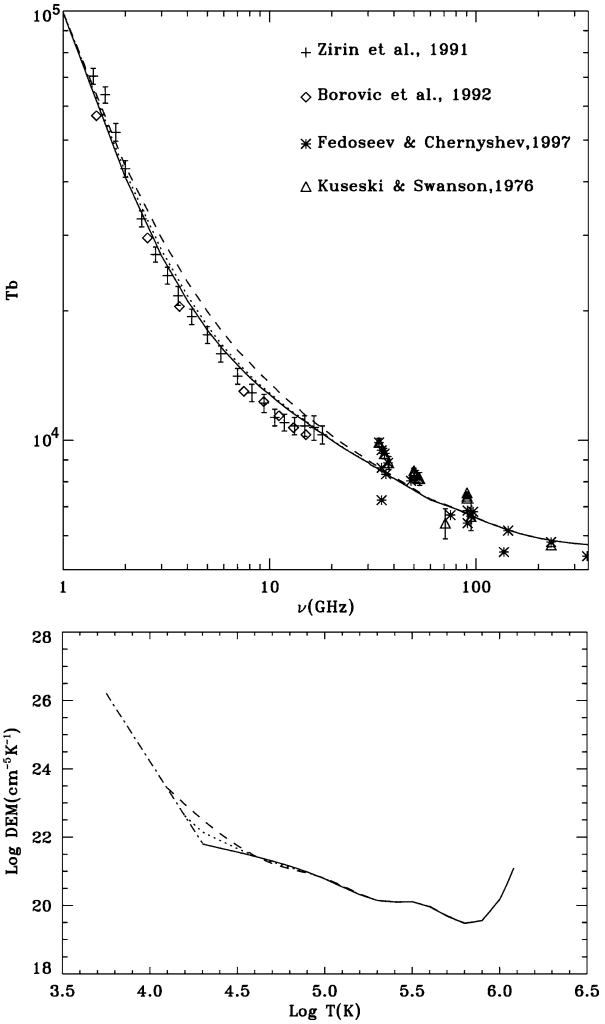


**Figure 4** Spectra computed by Landi and Chiuderi Drago (2008) (top) and the corresponding differential emission measure DEM (bottom). Reproduced by permission of the AAS.

In other studies, a profound decrease in the computed temperatures have been obtained by assuming a tail of suprathermal electrons present in the solar atmosphere. Chiuderi and Chiuderi Drago (2004) modeled this with a two-component Maxwellian electron distribution and with a so-called kappa-function, and found both working. More recently, the non-thermal $\kappa$-distributions have been found to change EUV filter responses quite significantly (Dudík *et al.*, 2009), further suggesting a need to revise the atmospheric models.

At longer (metric) wavelengths there is a marked departure of observed brightness temperature below the coronal electron temperature; moreover, the brightness temperature shows a maximum of $\leq 10^6$ K near 2 – 3 m (see Figures 4 and 5 of Lantos, 1999). This is attributed to refraction and scattering effects. Thejappa and MacDowall (2008) used Monte Carlo simulations to show that the one-order of magnitude lower-than-predicted brightness temperatures at low frequencies could be due to scattering of the quiet Sun emission by random density fluctuations.

## 3. High-Resolution Imaging Observations

### 3.1. From Microwaves to Sub-millimeter Waves

Low spatial resolution is a well-known obstacle for radio observations. It is, therefore, not surprising that solar radio astronomers exploit every possibility to use the most powerful aperture synthesis instruments available. In this context, Kundu *et al.* (1979) were the first to obtain quiet Sun images at 6 cm wavelength with arc-second resolution with the Westerbork Synthesis Radio Telescope (WSRT), after its successful use for active region studies (Kundu and Alissandrakis, 1975a) and following a number of interferometric (see, *e.g.*, Kundu and Velusamy, 1974; Kundu and Alissandrakis, 1975b) and one-dimensional (see, *e.g.*, Bogod and Korolkov, 1975; Gelfreikh *et al.*, 1977) observations of the QS.

The first WSRT quiet Sun images showed a clear association of the microwave emission with the chromospheric network, something that had already been suggested on the basis of interferometric data (Kundu and Alissandrakis, 1975b). This conclusion was subsequently verified with the Very Large Array (VLA) observations at 6 and 20 cm by Gary and Zirin (1988), and by Gary, Zirin, and Wang (1990) at 3.6 cm. In the mid 90's the VLA was used for quiet Sun observations in the short cm-range (1.2, 2.0 and 3.6 cm) by Bastian, Dulk, and Leblanc (1996), Benz *et al.* (1997), and Krucker *et al.* (1997).

At present, the Nobeyama Radioheliograph (NoRH, Nakajima *et al.*, 1994) carries out full-disk routine observations of the Sun at 17 and 34 GHz. NoRH has been operating since 1992, with only a two-month gap in observations in 1995. The available data cover almost 18 years, and observations run eight hours per day with one-second time cadence. The Siberian Solar Radio Telescope (SSRT, Grechnev *et al.*, 2003) is also performing two-dimensional mapping, concurrently with one-dimensional images obtained in the additive mode, since 1996 at 5.7 GHz. The correlation mode with high-sensitivity permits low-contrast features on the Sun to be investigated.

High-resolution images of the quiet Sun in the mm-range were first produced by White, Loukitcheva, and Solanki (2006) and Loukitcheva, Solanki, and White (2006). They used the 10-element Berkeley–Illinois–Maryland Association Array (BIMA) in its most compact D-configuration, to obtain $\sim 10''$ resolution. BIMA was followed by CARMA (Combined Array for Research in Millimeter-wave Astronomy, a fusion of BIMA and OVRO) and White (communication at the CESRA 2010 meeting, La Roche-en-Ardenne, Belgium) used the 15-element array to observe the quiet Sun at 3.3 mm. In both cases extreme care was taken to minimize atmospheric effects and image reconstruction problems.

BIMA and CARMA images at 3.5 and 3.3 mm wavelengths are shown in Figure 5, together with VLA images at 1.3 and 2.0 cm, for comparison. In all cases the chromospheric network, delineated in the TRACE continuum images or the photospheric magnetograms, is the dominant structure in the radio images. Network structures appear broader in radio, but this effect almost disappears if one degrades the TRACE images to the resolution of the radio images.

### 3.2. Metric Range Imaging

There is a noticeable lack of imaging in the decimetric range, from 30 cm (1 GHz) to 70 cm (450 MHz). At the long wavelength end of the spectrum one has to be content with arc-minute resolution. Moreover, the Sun must be without any burst activity if the quiet Sun component is to be imaged.

The first images in the metric range were obtained with the now-extinct Culgoora Radioheliograph at 80 MHz (3.75 m) and 160 MHz (1.88 m), followed by the also extinct Clark

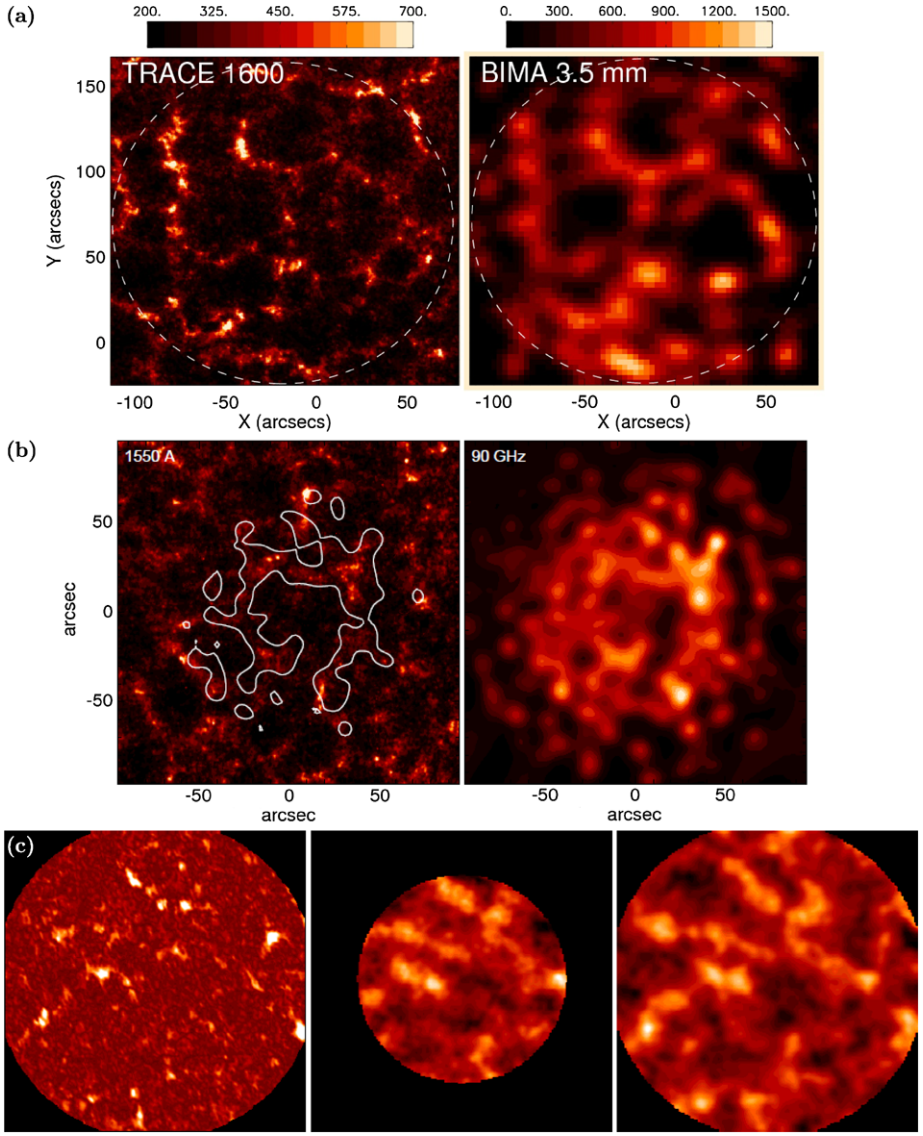


**Figure 5** High-resolution radio images of the quiet Sun in the mm-wave to short cm-wave range. (a): TRACE 1600 Å image together with the BIMA radio image at 3.5 mm (85 GHz) on May 18, 2004 (adapted from Loukitcheva, Solanki, and White, 2010, reproduced with permission © SAIt); (b): TRACE 1550 Å image together with the 3.3 mm (90 GHz) image obtained with CARMA on September 26, 2008 by White (communication at the CESRA 2010 meeting, La Roche-en-Ardenne, Belgium) and (c): Image of the absolute value of the photospheric magnetic field from KPNO (left), together with VLA radio images at 1.3 cm (23 GHz, middle) and at 2.0 cm (15 GHz, right) on September 23, 1992 (adapted from Bastian, Dulk, and Leblanc, 1996, reproduced by permission of the AAS). Fields of view are 195″by 195″ in (a), 190 by 190″ in (b) and 165 by 165″ in (c). The spatial resolution is 12″ for the mm-wave images in (a) and (b), and 3.3″ and 5″ at 1.3 and 2 cm, respectively, in (c). The dashed circles in (a) show the 96″ radius of the BIMA field-of-view where the fluxes were estimated to be reliable.

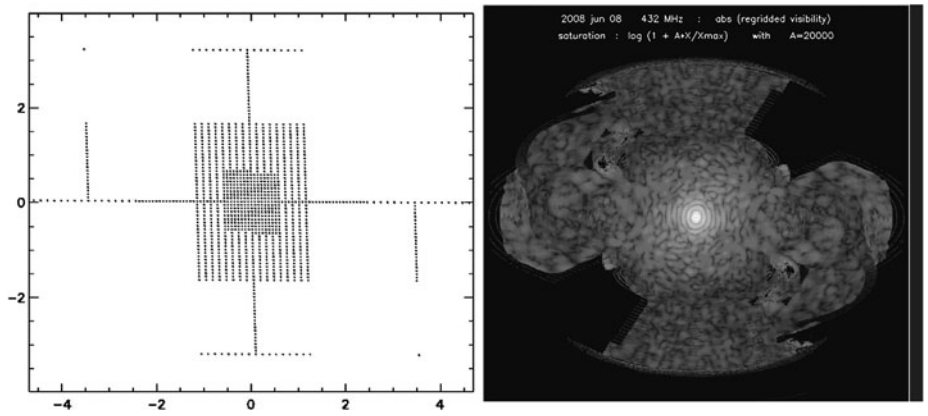


**Figure 6** (a) Instantaneous coverage of the $u$–$v$ plane by the Nançay Radioheliograph. The units are in $10^3$ rad$^{-1}$ (adapted from Mercier and Chambe, 2009, reproduced by permission of the AAS). (b) Gridded amplitude of the visibility function after six hours of synthesis at 432 MHz on June 8, 2008. Amplitude values cover a range of five orders of magnitude (Mercier, communication at the CESRA 2010 meeting, La Roche-en-Ardenne, Belgium).

Lake Radioheliograph at 73.8 MHz (4.07 m), 50 MHz (6 m) and 30.9 MHz (9.7 m). The Nançay Radioheliograph (NRH) operated as two independent arrays (E–W and N–S) at 169 MHz (1.78 m) until Alissandrakis, Lantos, and Nicolaidis (1985) employed aperture synthesis to combine 6 hours of observations into a 2D-image with 1.2′ by 4.2′ resolution.

The NRH has evolved gradually to its present state of 2D synthesis instrument (Kerdraon and Delouis, 1997), providing images at 10 frequencies from 450 to 150 MHz (67 cm to 2 m) with a cadence of 0.25 sec. The instantaneous images, however, cannot exploit the full resolution of the system but only use the densely sampled inner part of the $u$–$v$ plane, see Figure 6. In order to exploit the full resolution one has to resort to full-day synthesis, which improves the resolution by a factor of $\sim 2.5$. This was done by Marqué (2004) with an emphasis on filament cavities and, more recently, by Mercier and Chambe (2009) in a systematic study of the quiet Sun. They used self-calibration and a modified CLEAN algorithm to correct and process the NRH visibilities. We note that Mercier *et al.* (2006) also computed instantaneous burst images at 327 MHz by combining NRH and Giant Metrewave Radio Telescope (GMRT) data.

Figure 7 shows some examples of synthesis images from Mercier and Chambe (2009), together with earlier work by Marqué *et al.* (1999) and a set of 1992 images from Lantos (1999). The NRH covers a broad range of frequencies, the ratio of the maximum to minimum frequency being $\sim 3$; it can thus probe an altitude range from the upper TR to the low corona. The altitude range goes lower in coronal holes. They are the most prominent feature at long dm wavelengths and, in agreement with previous observations (see, *e.g.*, Lantos *et al.*, 1987), their contrast decreases at longer wavelengths (see Section 4.5).

## 4. Observations and Interpretation of Quiet Sun Features

### 4.1. Center-to-Limb Variation

In the optical range, the decrease of temperature with height in the photosphere leads to the well-known limb darkening effect. In contrast, the temperature rise in the chromosphere and

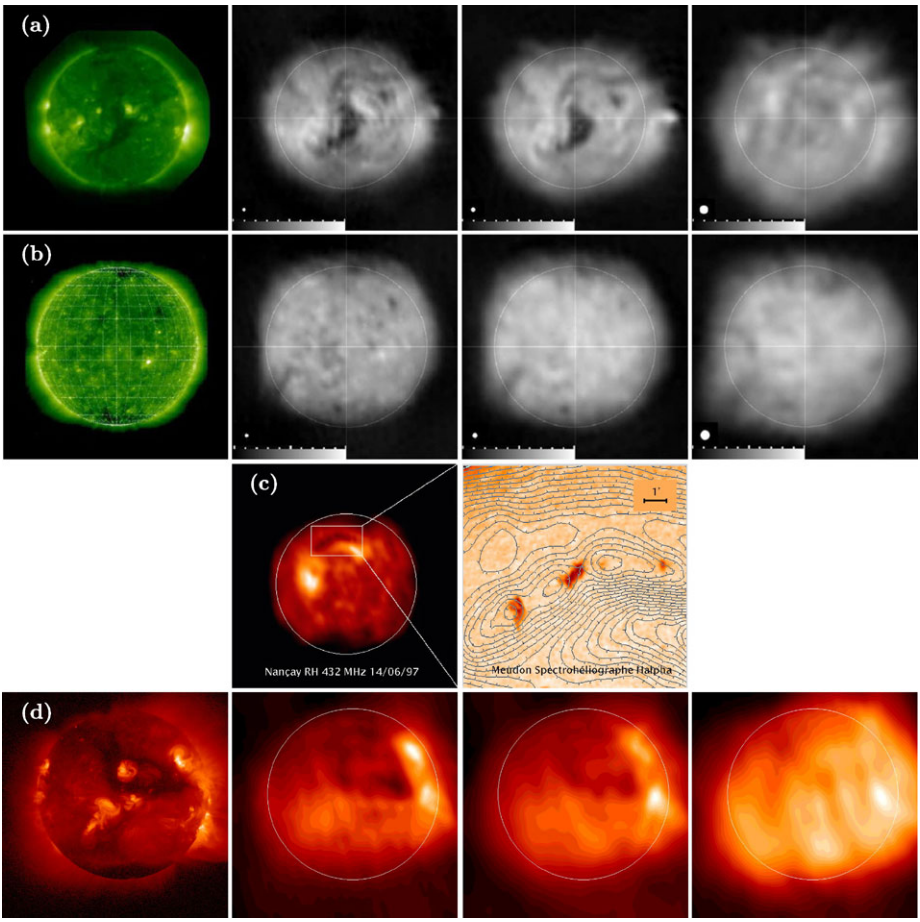


**Figure 7** Synthesis images with the Nançay Radioheliograph: (a) Images at 432, 327 and 164 MHz on June 27, 2004, together with a GOES SXI image; (b) Images at 432, 327 and 173 MHz on June 6, 2008, together with an EIT 195 Å image; (c) Image of a filament at 432 MHz and Hα, and (d) Images at 432, 327 and 410 MHz on May 26, 1992, together with a *Yohkoh* SXT image. White dots in (a) and (b) show the resolution. (a) and (b) were adapted from Mercier and Chambe (2009), reproduced by permission of the AAS, (c) from Marqué *et al.* (1999), and (d) from Lantos (1999).

the corona is expected to cause limb brightening at radio wavelengths. Thus observations of the radio brightness variation from the disk center to the limb provide a good test for solar atmospheric models.

These conclusions are valid if the atmosphere is stratified, *i.e.* the temperature increase/decrease depends only on height. However, the actual solar atmosphere has complicated structures such as spicules and loop-like structures, filled with low or high temperature plasma. For example, Belkora *et al.* (1992) measured the solar limb brightness profile at 3 mm during a solar eclipse and found a close correspondence between the 3-mm limb profile and the height of H$\alpha$ spicules.

It is therefore no surprise that the observed center-to-limb variation shows less brightening than the homogeneous models predict, or even shows darkening, which cannot be attributed to the limited instrumental resolution. This is usually interpreted in terms of ab-

sorbing features, such as chromospheric spicules (see, *e.g.* Lantos and Kundu, 1972). More recently, Selhorst, Silva, and Costa (2005) calculated the brightness distribution at 17 GHz with an atmospheric model they developed and obtained a too-sharp brightening around the limb, even after convolving with the instrumental beam. This changed drastically when they introduced spicules. They could then successfully fit the observed east–west brightness profiles with the model.

Enhanced limb brightening causes an increase of the solar disk size observed in radio. Selhorst, Silva, and Costa (2004) measured the solar radius at 17 GHz using images taken by the NoRH and showed a $3''$ variation of mean radius during one solar cycle, which is smaller than previous studies. Recently, Krissinel (2005) used SSRT observations to derive two-dimensional brightness distributions and to calculate the radio radius as a function of position angle for several wavelengths from 4 to 31.6 cm.

Limb brightening shows solar activity dependence due to the change of structure of the upper atmosphere. The radio limb is enhanced when active regions are closer to the limb. Not only active regions, but also the polar atmosphere depends on solar activity, as discussed in the following subsection.

### 4.2. Polar Brightening

Polar regions are brighter than the low-latitude quiet Sun at short cm-waves to mm-waves. This phenomenon was found by Efanov *et al.* (1980), and it was confirmed by Kosugi, Ishiguro, and Shibasaki (1986) with higher spatial resolution observations. The brightness in the polar regions can reach that of active regions. Many studies, including these two, have been carried out to find counterparts of the radio brightening at other wavelengths, see *e.g.*, Nindos *et al.* (1999), Pohjolainen, Portier-Fozzani, and Ragaigne (2000), and Selhorst *et al.* (2010). Figure 8 shows one example of the observed brightness enhancements. General agreement so far is that the radio brightness in polar regions is anti-correlated with solar activity, represented by sunspot numbers. Polar faculae have similar activity dependence, but no one-to-one correspondence has been found between faculae and radio bright patches (see, *e.g.*, Riehokainen *et al.*, 2001).

The annual variation of averaged polar brightening was studied by Shibasaki (1998), who found that averaged polar brightening consists of two components; one depends on the distance to the limb and the other depends on the distance to the poles. This can be seen by plotting north–south brightness distribution with and without $B_0$, heliographic latitude of the disk center, correction. Both plots have annual variation with similar amplitude. This result can be interpreted as follows: The averaged polar brightening is a limb brightening and it is modulated by the distance from the poles due to $B_0$ variation.

Around solar activity minimum, polar regions are dominated by strong unipolar magnetic field and hence the magnetic field lines are expected to be radial. Under such conditions, we can assume that the atmosphere is mainly in stratified structure with a smaller number of closed loops and/or tilted spicules filled with low temperature plasma. As the strong unipolar field is associated with the solar polar regions, limb brightening will be modulated annually by $B_0$. In contrast, during solar activity maximum the polar magnetic field becomes weak and changes its polarity. This means that unipolar field will be suppressed and complex magnetic field dominates. Under this condition, we expect that limb brightening will be suppressed. This can explain the anti-correlation of polar brightening with solar activity.

For systematic studies of solar cycle dependence of polar brightening, long-term full-disk observations are necessary. Daily images taken by NoRH can be used for such studies, and for example Shibasaki (1998) synthesized a radio butterfly diagram by using images from

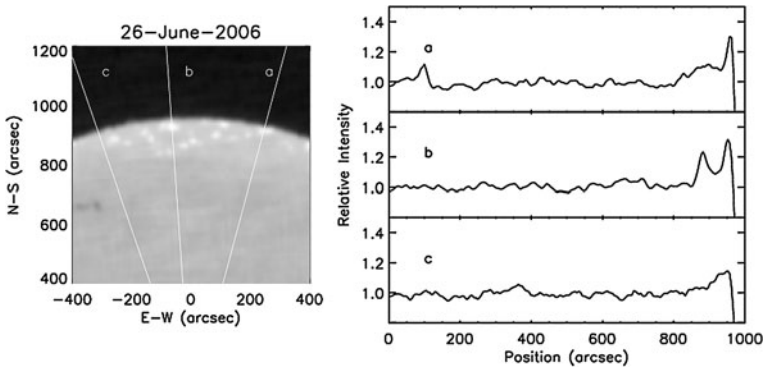


**Figure 8** Bright patches are observed near the north pole during solar activity minimum at 17 GHz (NoRH observations). White lines represent three scans in the map, the profiles of which are shown on the right. Scan (a) goes through one bright patch, scan (b) through two patches, and scan (c) shows only the background limb brightening (Selhorst *et al.*, 2010, reproduced with permission © ESO).

**Figure 9** Radio butterfly diagram synthesized from daily NoRH images between 1992 and 2010 at 17 GHz.

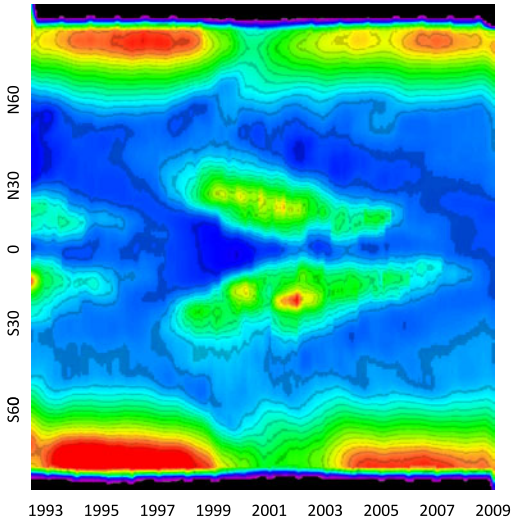


half a solar cycle. He found a systematic increase of the bright polar area as the solar activity declined.

At present, 18 years of NoRH imaging data are available, and Figure 9 shows a butterfly diagram with 17 GHz data taken between 1992 and 2010. To suppress annual variation, one-year running mean values were used in constructing the plot. In the diagram, we can clearly see that polar brightening is anti-correlated with low-latitude activities. In this display, polar regions are much brighter than active regions due to averaging along longitude. From the diagram, we notice easily the north–south asymmetry, as the southern pole is brighter than the northern pole. It can also be noticed that the polar brightness during activity minimum, between solar Cycles 23 and 24, is weaker than that during the previous minimum, at both poles. This suggests that the polar magnetic field during Cycles 23 – 24 minimum is weaker than that of Cycles 22 – 23 minimum. At lower latitudes, we notice the long delay of the appearance of active regions in the 24th Cycle. There must be some relation between the

magnetic field in the polar regions and in the active region belts. It will be most useful to follow how the solar Cycle 24 will develop and to study the link between cycles.

### 4.3. Chromospheric Network, Transient Phenomena and "Heating" Events

The observational aspects of the network were treated in Section 3.1. In addition to the spatial coincidence of bright radio features with the chromospheric network, it is important to measure the intensity and size of the bright features as a function of wavelength. We should note that interferometric/synthesis observations cannot measure the background level, which should be provided by other means. Thus, the most appropriate measure of the intensity fluctuations is their amplitude or, even better, their rms variation.

In all reported measurements both the amplitude and the rms increase with wavelength. According to Benz *et al.* (1997), the rms varies from 290 K at 1.3 cm to 930 K at 3.6 cm; these values are consistent with the ones given by Bastian, Dulk, and Leblanc (1996) at 1.3 and 2 cm and they correspond to 2.8% and 5.8% variations, respectively, if reasonable values for the background are considered. The actual increase should be larger, due to the decrease of spatial resolution with wavelength. At 6.1 cm, Gary and Zirin (1988) give 8300 K and 21400 K above the background as the average value of individual source peak brightness in two regions, while Kundu *et al.* (1979) give absolute values of $\sim 2.5 \times 10^4$ and $\sim 1.5 \times 10^4$ K for typical network elements and cell interiors, respectively, at 6 cm. In the mm range, Loukitcheva, Solanki, and White (2009) give 1100 K for the intensity variation.

These results have not been fully exploited in multi-component models. Older computations by Chiuderi Drago, Kundu, and Schmahl (1983), based on the Vernazza, Avrett, and Loeser (1981) model, do show an increase of brightness difference between network and cell interiors with wavelength, while the values reported in recent works are close to those computed by the above authors for the VAL model D (average network).

It is well known from EUV data that the network becomes diffuse in the upper transition region and disappears in the low corona, thus a similar behavior is expected for the radio network. The main problem here is the variable spatial resolution. Bastian, Dulk, and Leblanc (1996) reported no detectable change between 1.3 and 2 cm, after smoothing the 1.3 cm image to match the 2 cm resolution. There is a spectral gap between 6 and 20 cm; however, the few published QS images at 20 cm (see, *e.g.* Gary and Zirin, 1988, see also the 20 cm image in Figure 3) do not show much of a network.

It is fairly well established (Erskine and Kundu, 1982; Bastian, Dulk, and Leblanc, 1996) that the radio fine structure presents time variability comparable to that of the chromospheric network, on time scales of minutes to hours. Apart from that, it is important to check for oscillatory behavior, which could be a signature of shock waves heating the upper solar atmosphere. This is not an easy task, due to the inherent difficulties in the instantaneous mapping of complex structures.

In the mm-wavelength range, White, Loukitcheva, and Solanki (2006) reported intensity oscillations (actually wave trains lasting typically for 1 – 3 wave periods) in the frequency range 1.5 – 8 mHz (periods of 125 – 700 s), with rms brightness variation of 50 – 150 K; they noted that network regions had a tendency to exhibit longer period oscillations than the internetwork.

A number of authors have also looked for impulsive/transient events that may have a bearing on the heating of the upper atmosphere, as signatures of magnetic reconnection. Note that the radio range is very sensitive to small non-thermal electron populations that are expected as a by-product of the reconnection process. We must also note that impulsive brightenings might be associated with X-ray bright points rather than with the network

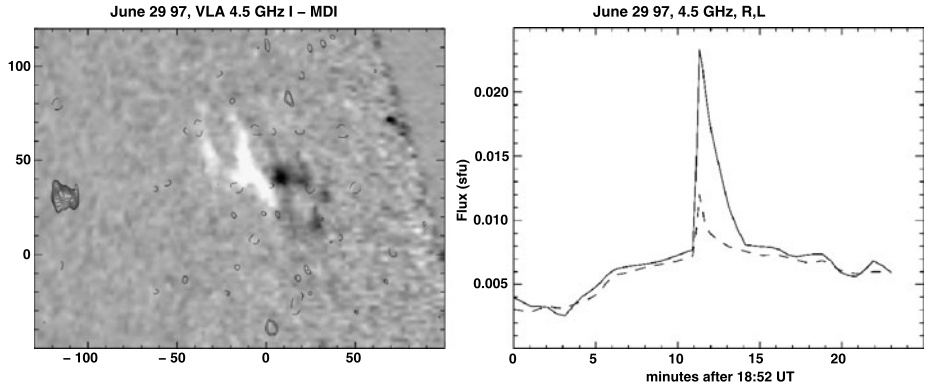


**Figure 10** Left: Contours of a transient brightening at 4.53 GHz observed by the VLA, overlaid on an MDI magnetogram (axes are in arc seconds). Right: time profiles of right- and left-hand polarized microwave emission (solid and dashed lines). The event occurred well away from any active region and had no associated soft X-ray emission (adapted from Nindos, Kundu, and White, 1999, reproduced by permission of the AAS).

proper; moreover, the limited spatial and temporal resolution could make it difficult to discriminate between a single source and multiple sources and this will have a bearing on the number of sources detected.

In this context, Krucker *et al.* (1997) detected four Yohkoh soft X-ray events associated with radio emission at 2 cm in 10 s VLA snapshot images; they estimated that roughly one such event occurs on the Sun every 3 seconds, all together providing a total power of $\sim 2 \times 10^{25}$ erg s$^{-1}$, which is five times less than the total power radiated by the quiet corona in X-rays. They also estimated the number of radio sources without any associated soft X-ray emission to be about 10 000 at any given time on the Sun, which appear at a rate of about 20 per second. In a similar study Gary, Hartl, and Shimizu (1997), using one OVRO antenna and Yohkoh SXT images, found that only 5 out of 35 transient brightenings detected with SXT in an active region had no radio counterpart; they also found a delay of 1 to 2 min of the X-ray peak with respect to the radio. The relative timing of events was also studied by Benz and Krucker (1999), using data at 2, 3.6, and 6 cm from VLA together with EIT, CDS and SUMER data from SOHO. They found that the radio peaks preceded the coronal emission and lagged behind O V emission (see also Krucker and Benz, 2000).

Some of these transient events have flare-like characteristics. Indeed, there appears to be a continuity between bursts, the radio counterparts of X-ray bright points (see Keller and Krucker, 2004, and references therein), and smaller events such as those described in the previous paragraph. Transient brightenings are observed in microwaves both within and well away from any active regions (Figure 10), and both thermal and non-thermal emission mechanisms have been suggested (White *et al.*, 1995; Nindos, Kundu, and White, 1999). Selection methods may have influenced these findings, as the thermal transient brightenings in microwaves were selected on the basis of their simultaneous soft X-ray emission, and the non-thermal brightenings were microwave-selected. In any case, it seems evident that electrons are accelerated to non-thermal energies even in the quiet solar atmosphere.

Short-duration, isolated metric radio bursts that are not associated with any radio continuum (noise storms) and are located outside active regions have been reported (Crosby *et al.*, 1997; Ramesh *et al.*, 2010). The burst locations have been resolved from radioheliograph images, but no counterparts have been found when compared with X-ray, EUV, and

UV structures or events. Further analysis would require simultaneous high time-resolution imaging data at all wavelengths.

Decametric radio observations present numerous faint frequency-drifting emissions, similar to "solar S bursts" reported by McConnell (1982). No specific relationship between the occurrence of these emissions and the solar cycle or presence of flares have been found (Briand *et al.*, 2008). Briand *et al.* (2008) suggest that a moderate, localized, time-dependent heating leads to low velocity electron clouds, which can in turn generate Langmuir waves and electromagnetic signals by nonlinear processes.

### 4.4. Solar Rotation and Tracers

Structures visible at radio waves can be used to determine solar rotation rates and source heights, especially at high solar latitudes. Since the radio structures are located in the solar chromosphere and corona, projection effects play a role in the position determination. Thus, Alissandrakis, Lantos, and Nicolaidis (1985) measured a height of $0.23\,R_{\odot}$ for emission sources at 169 MHz. A method of solar rotation stereoscopy was developed by Aschwanden and Bastian (1994), to enable height determination. The method was tested on Owens Valley microwave data (Aschwanden *et al.*, 1995), which showed that the height dependence of the coronal magnetic field and the plasma temperature can be inverted from the stereoscopic altitude spectra and the observed brightness temperature spectra.

Later, Rosa *et al.* (1998) developed a method for the simultaneous determination of the solar synodic rotation velocity and the tracer height. Using this method, Brajša *et al.* (2009) determined that the low brightness-temperature regions observed at 8 mm wavelength were located at heights of about 45 600 km. These heights are in agreement with filament heights, but disagree with our current understanding on coronal hole structures. Brajša *et al.* also concluded that thermal bremsstrahlung can explain both the brightness temperature depressions (prominences and coronal condensations) and enhancements (ordinary active regions). Brajša *et al.* (2000) found earlier that the differential rotation of brightness depressions is more rigid than that obtained tracing magnetic features and measuring Doppler shifts. There were also cycle-related changes and north–south asymmetry in the measured solar rotation velocities.

### 4.5. Coronal Holes, Streamers, and Filaments

Coronal holes are regions of lower density and therefore they are usually observed as brightness depressions at radio wavelengths (*e*.g., Lantos and Alissandrakis, 1999; Borovik and Medar, 1999). At mm- and cm-waves, the average brightness temperature of coronal holes is not much different from the quiet Sun. Both diffuse emission and local brightness enhancements inside some of the holes and at coronal hole borders have been observed (Kosugi, Ishiguro, and Shibasaki, 1986; Gopalswamy *et al.*, 1999; Pohjolainen, Portier-Fozzani, and Ragaigne, 2000; Moran *et al.*, 2001; Riehokainen, Valtaoja, and Pohjolainen, 2003). Increased H$\alpha$ brightness was detected inside some equatorial coronal holes that also showed enhanced radio emission, see Figure 11, but comparisons to UV and EUV line observations did not reveal any correspondence (Moran *et al.*, 2001). However, the inadequate spatial resolution of single-dish radio observations and the difficulty of interferometers to resolve faint diffuse sources have made these comparisons difficult.

Magnetic network elements, similar to those responsible for the enhanced radio emission in bright points (Benz *et al.*, 1997), have been suggested as the origin for coronal hole brightenings. The electron-cyclotron maser mechanism has been excluded as a possibility,

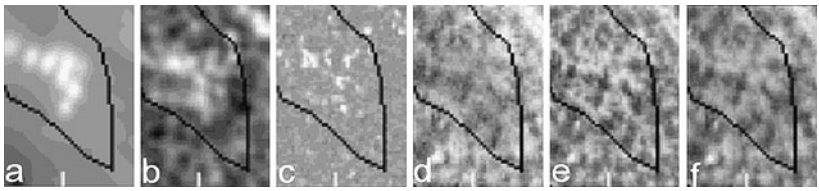


**Figure 11** Radio-bright structures observed inside an equatorial coronal hole: (a) NoRH observations at 17 GHz, compared with (b) BBSO H$\alpha$ image, (c) MDI magnetogram, and (d) – (f) selected UV spectral lines observed by SUMER. (Figure adapted from Moran *et al.*, 2001, reproduced with permission © ESO.)

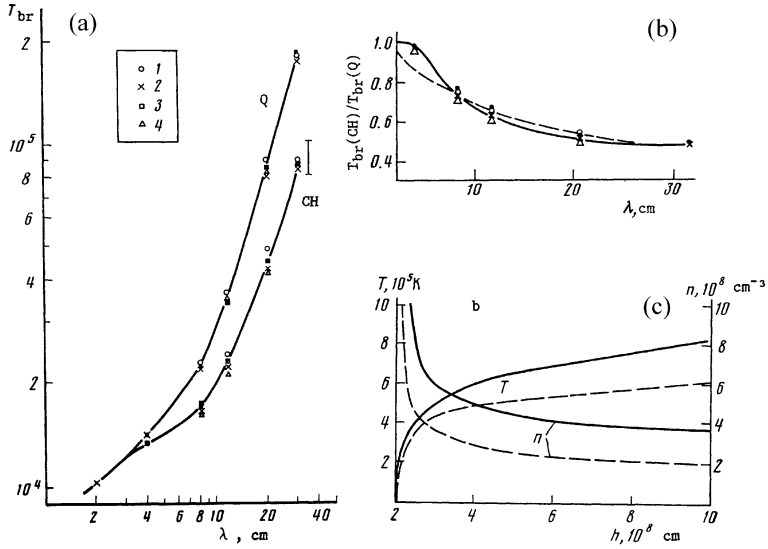


**Figure 12** (a): RATAN-600 measurements of the brightness temperature for the quiet Sun (Q) and coronal holes (CH). (b): the contrast of coronal holes with respect to the quiet Sun, the dashed line shows the model computations. (c): the corresponding electron temperature and density models. (Adapted from Borovik *et al.*, 1990.)

as it is not able to provide significant radio wave emission from the coronal funnels at the supergranular network (Vocks and Mann, 2004). Krissinel *et al.* (2000) proposed that a difference in the electron density and temperature in different holes and in different parts of a hole can account for the variable brightness temperatures. They also noted that the influence of these parameters is strongest in the 2 – 5 cm wavelength range. A recent study by Brajša *et al.* (2007) suggests that an increased density in the transition region and low corona could explain both the brightness temperature enhancements and depressions at millimeter waves.

A number of computations of the coronal hole radio emission (see, *e*.g., Borovik *et al.*, 1990; Chiuderi Drago *et al.*, 1999) and calculations of the expected brightness temperatures (see, *e*.g., Pohjolainen, 2000) have been published. Figure 12 shows the RATAN-600 spectral observations of four coronal holes in the wavelength range of 2 to 32 cm, together with quiet Sun data; the brightness difference between the two becomes appreciable above $\sim 4$ cm. In the best-fit models the coronal holes are cooler than the background and less dense by a factor of two. Mercier (communication at the CESRA 2010 meeting, La Roche-en-Ardenne, Belgium) presented measurements obtained with the NRH from 70 cm to 1.8 m,

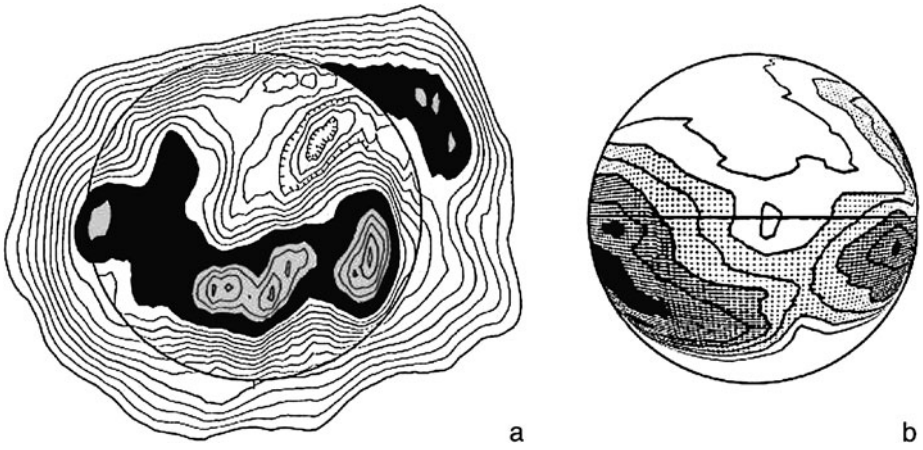


**Figure 13** (a): NRH map of the Sun at 169 MHz on July 15, 1984. The black region is the *coronal plateau*. A coronal hole is marked by hatched contours. (b): The corresponding K-corona synoptic map, on spherical projection. From Lantos and Alissandrakis (1999), reproduced with permission © ESO.

together with models that assumed isothermal corona and chromosphere in hydrostatic equilibrium with no transition region. They, too, found a density decrease in the holes by a factor of two with respect to the quiet Sun.

At decameter waves coronal holes are sometimes seen in emission, Dulk and Sheridan (1974) reported such a case. Lantos *et al.* (1987) observed a bright emission source at decametric wavelengths, located above an extended coronal hole, in a region where a depression was seen at meter waves. A possible interpretation is in terms of refraction effects (Alissandrakis, 1994, *cf.* Figure 3 of Lantos, 1999) and/or scattering in inhomogeneities.

In a systematic study of emission sources observed with the NRH at 169 MHz, Lantos and Alissandrakis (1999) came to the conclusion that the large-scale emission is dominated by the *coronal plateau* (Figure 13). This is an intermediate brightness area forming a belt around the Sun and surrounding almost all local emission sources (Lantos, Alissandrakis, and Rigaud, 1992). It is visible both in daily images and in synoptic charts, and has a close association with the coronal plasma sheet observed with K-corona instruments (Figure 13b). The diffuse emission of the *coronal plateau* could be due to a high altitude loop system which overrides the principal neutral line of the general solar magnetic field at the base of the heliosheet, with a possible contribution of loops connecting active regions to surrounding quiet areas. The same authors reported that medium scale local sources include both faint noise storm continua and thermal sources. Most of the latter are located between faculae and neutral lines, possibly in the upper leg of large-scale loops. A small number of thermal sources is closer to neutral lines, which might be loops at the base of isolated coronal streamers.

Coronal streamers are best visible at decametric wavelengths (see Lantos, 1999). They are less prominent in the meter and decimeter ranges, where one sees loops at the base of streamers rather than proper streamers, as pointed out in the previous paragraph. From the circularly polarized thermal emission of streamers observed with the Gauribidanur radioheliograph at 77 and 109 MHz, Ramesh, Kathiravan, and Sastry (2010) were able to estimate magnetic field strengths in the range of 5 – 6 G at 1.5 – 1.7 solar radii.

Large filaments are observed as depressed regions within the solar disk at mm- and cm-waves (Chiuderi Drago, 1990) and sometimes at decimeter-meter waves (Marqué *et al.*,

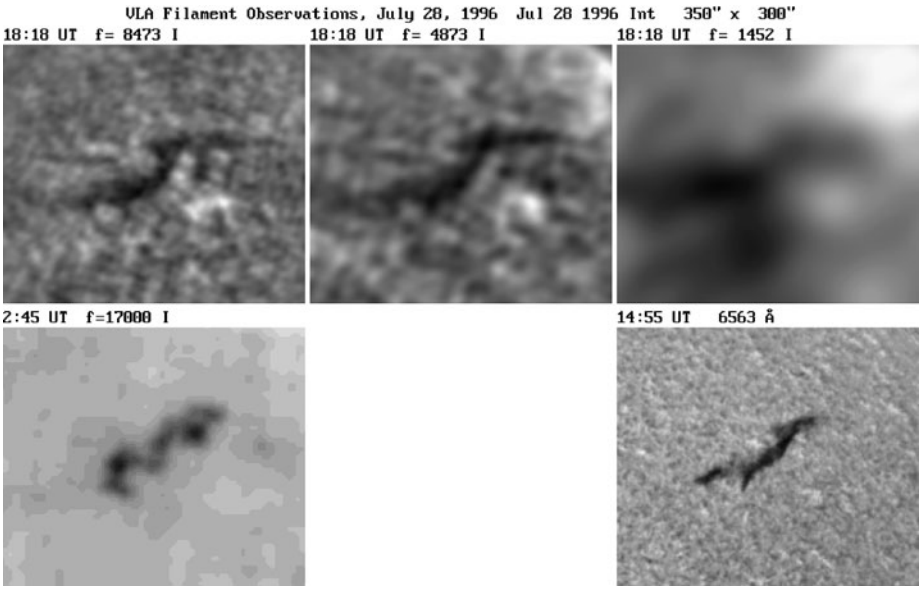


**Figure 14** A filament observed at radio wavelengths (VLA and NoRH) and in Hα. From Chiuderi Drago *et al.* (2001).

1999; *cf.* Figure 7c, Section 3.2). Above the limb, projected against the sky, filaments are seen in emission. It is possible to calculate electron temperatures and densities within the filament using multi-frequency radio observations (Irimajiri *et al.*, 1995), especially when the filaments erupt. A systematic study of the filament environment in the metric radio range was presented by Marqué (2004), where it was concluded that the most likely source of the radio depression is the cavity that surrounds the filament. The on-the-disk filament observations at microwaves, analyzed by Chiuderi Drago *et al.* (2001), see Figure 14, support a prominence model of cool threads embedded in the hot coronal plasma, with a sheath-like TR around them.

## 5. Active Regions

Active region associated emission dominates in the cm range. The main emission mechanisms of non-flaring active regions are the gyro-resonance radiation above sunspots and the free–free radiation from hot plasma trapped in active region loops. Both emissions are due to thermal electrons. We note, however, that quasi-steady non-thermal emission has been invoked in the interpretation of *peculiar sources* on top of neutral lines of the magnetic field (Alissandrakis *et al.*, 1993) and the *decimetric halo component* (Gelfreikh, 1998). At longer decimetric and metric wavelengths no sunspot-associated emission is visible, presumably due to the high opacity of the overlaying plasma and refraction effects.

The gyro-resonance emission mechanism is unique to radio and it is a useful tool to study the atmospheric layers above sunspots and measure the magnetic field (Gelfreikh, 1998). The emission is generated in thin layers around iso-Gauss surfaces with magnetic field strength such that the observing frequency is equal to the second or third harmonic of the local gyro-frequency. Due to the high opacity of these layers, strong emission is observed if they are located in the transition region or the corona.

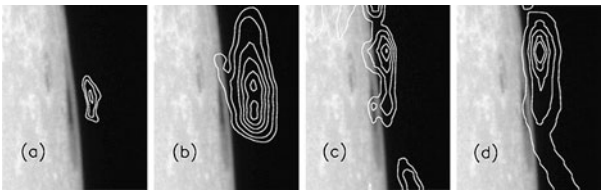


**Figure 15** Co-aligned white-light (TRACE), EUV (from CDS), and radio (VLA) observations of an active region near the solar limb: (a) 15 GHz, (b) 8 GHz, (c) O V, and (d) Ne VI intensity contours plotted over a white-light image (adapted from Brosius and White, 2006, reproduced by permission of the AAS).

The opacity (Kakinuma and Swarup, 1962; Zheleznyakov, 1962) is a complicated function of the temperature, the density, the intensity and the direction of the magnetic field and the wave mode. It is much higher in the extraordinary mode than in the ordinary one, it is also much higher at the second harmonic than at the third; thus, the third harmonic is opaque in the extraordinary and transparent in the ordinary mode, while the second harmonic is opaque in both modes.

Consequently, if the photospheric field strength is low enough (or the frequency is high enough) both harmonic layers are below the TR and no sunspot-associated emission is observed. For higher field or lower frequency, the third harmonic enters into the TR and strong, highly polarized emission is observed (Shibasaki *et al.*, 1994). For still higher field strengths the second harmonic also enters the TR and the polarization is reduced.

Due to the thin resonance layers and the strong dependence of the opacity on the angle between the line-of-sight and magnetic field, gyro-resonance sources show center-to-limb variation; the dependence of the source flux on the angular distance from the disk center can be described by a cosine curve with the top "cut off" (Borovik, Gelfreikh, and Lubyshev, 1975; Lubyshev, 1977). The level of the cut depends on the wavelength and increases at shorter wavelengths (Gelfreikh and Lubyshev, 1979). For example, at cm-waves the flux has a dip around the central meridian, making the source appear weak around the disk center, brighter at mid-distance, and weak again near the limb.

The strong radio emission over sunspots and sunspot groups has stimulated a large amount of theoretical and observational work over a long period of time, particularly after the first high-resolution observations by Kundu and Alissandrakis (1975a) and the first detailed modeling by Alissandrakis, Kundu, and Lantos (1980). Recent works on gyro-resonance emission are reviewed by White (2004) and Lee (2007).

A lot of recent work is based on NoRH imaging observations, and a consensus exists that at 17 GHz the gyro-resonance mechanism plays the most important role (Nindos *et al.*, 2000; Vourlidas, Gary, and Shibasaki, 2006; Selhorst, Silva-Válio, and Costa, 2008). At higher frequencies, imaging observations are more limited and the results are still inconclusive. The 34 GHz emission, for example, was successfully modeled as completely free–free radiation by Selhorst, Silva-Válio, and Costa (2008). At sub-mm waves, Silva *et al.* (2005) report a brightness excess of 3 – 20% over active regions and that the flux density spectra are increasing toward the THz range.

High-resolution multi-wavelength observations of sunspots can be used to test in detail the magnetic field model extrapolated from measurements at the photosphere (Lee *et al.*, 1998). For example, Brosius and White (2006) calculated coronal magnetic field strengths of 1750 G at a surprising large height (8000 km) above a large sunspot at the west solar limb, using radio observations from the VLA together with TRACE, CDS, EIT, and MDI observations (Figure 15). The observations can also provide valuable diagnostics of the ac-

tive region atmosphere and magnetic field, in particular if high spatial resolution spectral data are available (see, *e.g.* Tun, Gary, and Georgoulis, 2011).

Radio observations are valuable in providing information on temporal variations of the emission from active regions. Generally, signals of oscillations and waves are weak compared to the background quiet Sun and active regions, and intensity fluctuations caused by terrestrial atmosphere dominate. Radio interferometric observations can suppress atmospheric effects and 3-minute umbral oscillations of gyro-resonance sources are clearly observed by the NoRH (Gelfreikh *et al.*, 1999). Radio pulsations show a large variety of periods, bandwidths, amplitudes, temporal and spatial signatures, and on this extensive field of research we refer to the review by Nindos and Aurass (2007). Recently, Sych *et al.* (2010) found three-minute propagating waves in a sunspot observed with the NoRH and TRACE, near the footpoints of locally open magnetic field lines.

On long time scales, the total radio flux integrated over the whole disk is known to be a good index of solar activity, especially around 10 cm wavelength (2.8 GHz), as it shows good correlation with relative sunspot numbers, due to contributions from both emission components. The spectral peak of radio emission from non-flaring active regions is located around the 10 cm wavelength. Weather conditions such as clouds and rain do not influence the measurements at wavelengths longer than 10 cm, and ionospheric disturbances do not influence at wavelengths shorter than 10 cm. Therefore the 10 cm wavelength is favorable for accurate ground-based measurements because it is free from both influences. Also, a very robust absolute calibration method can be established (Tanaka *et al.*, 1973), to minimize the instrumental effects. Thus, it is possible to use the total radio flux as a long-term activity index of the Sun, similar to or even better than the relative sunspot numbers.

For studies of anomalous solar activity during and after the minimum period of the solar Cycles 23 and 24, total flux data will play an important role. More than 60 years of records with uniform calibration exist nowadays (Tapping *et al.*, 2007). Figure 16 presents averaged total flux measurements at four microwave frequencies between 1951 and 2010, observed by radio observatories in Toyokawa and Nobeyama in Japan.

## 6. Future Challenges

### 6.1. Atmospheric Structure and Dynamics

The radio data provide valuable information on the structure of the solar atmosphere above the temperature minimum. To this end reliable absolute measurements of the brightness temperature are required. The existing data show very much scatter, most prominent in the mm and sub-mm wavelengths which are formed below the TR. The scatter could be due to inherent difficulties in the measurements and/or solar cycle variations, although the latter are not expected to be very important at the relevant atmospheric layers. In any case, there is an obvious need for more consistent observations and these can only be obtained with single-dish instruments. Observations from space would be the ideal, since they are not hindered by the terrestrial atmosphere.

As pointed out in Section 2.2, a model can be found that fits most microwave data, the main problem being that the radio data are better fitted with models of the *cell interior*, rather than the average Sun. In addition to the fact that radio data are less affected by non-LTE effects and other uncertainties of the optical-UV range, this is probably due to different contributions of network and cell regions to the average intensity in the two domains. Indeed, Gary and Zirin (1988) estimated that the network contributes only 5 – 10% of the total brightness at 6 cm.

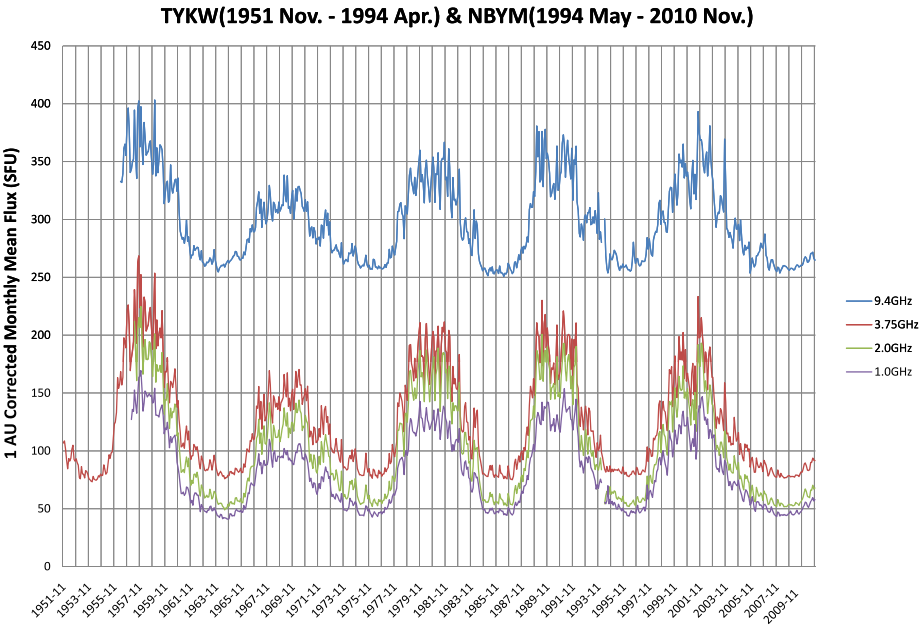


**Figure 16** Corrected monthly mean total solar flux at 1, 2, 3.75, and 9.4 GHz during 1951 – 2010 (Toyokawa and Nobeyama recordings).

There is a noticeable lack of multi-component atmospheric models that are based on observations of the network. The existing models are based on center-to-limb variations and employ absorbing structures, such as spicules, to explain the lack of brightening. Spicules, however, probably have *higher* temperature than the ambient chromosphere (*cf.* Beckers, 1972), so they could not be absorbing features. The limb darkening might be due to the ragged structure of the chromosphere-corona TR. In any case, the network/cell contrast and its variation with the wavelength could make the basis for a two-component model. Here we should point out again the lack of high-resolution observations in the range of 6 to 20 cm wavelength, which would reveal the gradual fading of the network in the upper TR and low corona.

The low value of the circular polarization in QS structures, combined with instrumental limitations, makes the measurement of the magnetic field in the network quite difficult. In coronal holes, Borovik, Medar, and Korzhavin (1999) reported values of 0.2 – 3% for the degree of polarization, and 2.5 – 10 G for the magnetic field. Surprisingly, they found an increase of the magnetic field with wavelength. Similar values, but at larger heights, have been reported for streamers (Ramesh, Kathiravan, and Sastry, 2010, see Section 4.5). Thus, there is a lot of important information to be obtained from improved measurements of circular polarization.

Radio observations can provide important input to the problem of the heating of the chromosphere and the corona, both in the wave and nano-flare heating scenarios (Section 4.3). Instruments with dense coverage of the $u$–$v$ plane as well as improved reconstruction techniques are necessary, in order to provide accurate instantaneous images of regions with complex structure.

The study of large-scale structures, such as coronal holes, loop systems, streamers and the *coronal plateau*, will benefit from systematic observations such as those with the NRH

(Section 3.2). Improved modeling in terms of refraction and scattering effects is also required.

Important diagnostics of active regions in the TR and the low corona, too many to be discussed here in detail, have been provided by radio observations. Still, the nature of apparently non-thermal, quasi-stationary emission sources remains unclear.

Finally, long time scales and synoptic aspects can be approached from the radio perspective, too. The total solar flux is an excellent index of solar activity (Figure 16), while radio butterfly diagrams show very well not only the migration of active regions toward the equator, but also the long-term behavior of polar brightening (Figure 9). It is thus important that such observations continue for the decades to come.

### 6.2. Instrumentation

The present-day solar radio instrumentation consists of single antennas and interferometer-aperture synthesis instruments. The antenna and receiver characteristics depend strongly on the wavelengths used. At millimeter waves and beyond, very good antenna surface accuracy and receiver stability is required. The Solar Submillimeterwave Telescope SST (Kaufmann *et al.*, 2008) uses a multiple beam technique to overcome the mapping limitations of a single-dish and single-receiver instrument. At long wavelengths like meter waves, much simpler and much more cost-effective techniques can be used. For example, the e-Callisto spectrometers (Benz *et al.*, 2009) have been installed at dozens of locations, with simple antenna structures, since the first installation in 2002.

The spatial resolution of a single antenna increases with the antenna size (*i.e.*, bigger antennas produce more narrow beams), which sets upper limits to fully steerable constructions. For example, the Nobeyama 45-meter diameter antenna has been used to image an eruptive prominence (Irimajiri *et al.*, 1995), but steering the antenna and scanning the solar disk with a $15''$ beam (at 110 GHz) proved to be very challenging. An example of a non-traditional design is the 600-meter diameter RATAN-600 reflector-type telescope, which can observe the Sun at high spatial resolution near the local noon. One-dimensional scans can be used to build two-dimensional maps (Nindos *et al.*, 1996) and from the observed circular polarization magnetic field strengths can be calculated (Akhmedov *et al.*, 1982).

Radio interferometers are providing high-resolution imaging at selected wavelengths. At present, there are only three solar-dedicated interferometers that observe the Sun on daily basis: NoRH, SSRT, and NRH (see Section 3). Also non-solar-dedicated interferometers, such as the WSRT and the VLA, have been used for solar observations regularly. We note, however, that general-purpose large radio interferometers have large elements and as a result their field-of-view is limited to a small part of the Sun. Dedicated solar radio interferometers consist of many small dishes to cover the full solar disk. Non-imaging total flux measurements also require small aperture dishes to cover the full solar disk uniformly.

To obtain imaging spectroscopy over a wide frequency range, a Frequency Agile Solar Radiotelescope (FASR) was designed in the early 2000. The Fourier synthesis telescope would provide such frequency, temporal, and angular resolution that both QS and flare observations are possible. Since then, the project has suffered from budget cuts, but the ongoing upgrade of OVSA and its use as a testbed will hopefully help to build FASR.

Of the new radio interferometers designed for astronomical use, the Low Frequency Array (LOFAR), the Murchison Widefield Array (MWA), the Long Wavelength Array (LWA), and the Atacama Large Millimeter/submillimeter Array (ALMA) can all be used for solar observations. The LWA, LOFAR, and MWA frequency ranges (10 – 90, 30 – 240, and 80 – 300 MHz, respectively) make them ideal for observing both the quiet Sun and solar

transients such as coronal mass ejections, but with the available spectroscopy (Oberoi *et al.*, 2011) also general plasma processes in the solar corona can be studied. We should note, however, that imaging at very low frequencies presents a significant challenge due to ionospheric effects. The ALMA frequency range, from 84 to 950 GHz, will open new opportunities in high-resolution imaging and spectroscopy at millimeter and submillimeter waves (Karlický *et al.*, 2011). Since the quiet Sun emission at these wavelengths originates from the chromosphere, ALMA observations will help refine atmospheric models (Sections 2.2 and 4.3).

### 6.3. Data Analysis

Many of the solar-dedicated radio instruments provide archives and data bases of their data. These databases can be used for various studies, such as flares, active regions, oscillations, prominence eruptions, quiet Sun and global solar cycle variations. The continued operation of instruments like the NoRH the SSRT and the NRH is essential both for case studies and long-term analysis and, not least, because the calibrated data are comparable independently of the year of observation. Especially for studies of anomalous solar activity during the rising phase of Cycle 24, well-calibrated uniform data covering more than one solar cycle are essential. After the long minimum of activity between Cycles 23 and 24, activity increases extremely slowly compared to previous cycles. Continuous full-disk observation by NoRH is very important.

The search for time variability in the quiet Sun radio emission has turned out to be a challenging task. With single-dish observations the flux is summed from the beam area where the antenna is pointing, and often simultaneous source tracking and source region imaging are not possible. Interferometers can overcome this problem but as they are less sensitive to the disk emission, new data analysis techniques have to be used for the deconvolution and building of images.

Many authors use a maximum entropy deconvolution technique, but this requires that there is significant flux present in the solar disk for a relatively long period of time (background positivity constraint). To completely resolve between cell interiors and network, we still need better deconvolution techniques and more closely-spaced antenna arrays.

Finally, it is important to develop tools for data analysis. For example, a web-based system for automated interactive detection of wave and oscillatory phenomena in imaging data sets was developed and tested with NoRH microwave maps and TRACE EUV images (Sych *et al.*, 2010; see also Section 5).

### 6.4. Concluding Remarks

In this review we have tried to present a picture, as complete as possible, of what the radio domain can tell us about the quiet Sun and active regions. In principle, the radio range can provide us with as much information as the rest of the spectrum for the solar atmosphere, from the temperature minimum up to the low corona; moreover, it can do that from the ground. A definite advantage of the radio range is that, for thermal processes as well for those non-thermal processes that are due to accelerated electrons, we understand the physics fairly well and we do not have to worry about such things as non-LTE effects, excitation and ionization equilibria, abundances, *etc.*, which are well-known burdens in the rest of the spectrum.

**Acknowledgements** The authors wish to thank the organizers and the participants of the CESRA2010 Workshop, which took place in La Roche-en-Ardenne in June 2010. This review took inspiration from the many presentations and working group discussions, as well as the more informal exchanges of ideas during the meeting. The authors also thank A. Nindos for his comments on the manuscript and the anonymous referee for careful review. Solar radio data were obtained from the archives of Nobeyama Solar Radio Observatory, at http://solar.nro.nao.ac.jp, and from the collaborative radio monitoring project at Paris Observatory-Meudon, at http://secchirh.obspm.fr/, and we thank their personnel for creating and developing these databases.

## References

Akhmedov, S.B., Gelfreikh, G.B., Bogod, V.M., Korzhavin, A.N.: 1982, *Solar Phys.* **79**, 41.
Alissandrakis, C.E.: 1994, *Adv. Space Res.* **14**, 81.
Alissandrakis, C.E.: 1999, In: Bastian, T., Gopalswamy, N., Shibasaki, K. (eds.) *Solar Physics with Radio Observations*, *NRO Report* **479**, 53.
Alissandrakis, C.E., Einaudi, G.: 1997, In: Trottet, G. (ed.) *Coronal Physics from Radio and Space Observations*, *Lecture Notes in Physics* **483**, 53.
Alissandrakis, C.E., Kundu, M.R., Lantos, P.: 1980, *Astron. Astrophys.* **82**, 30.
Alissandrakis, C.E., Lantos, P., Nicolaidis, E.: 1985, *Solar Phys.* **97**, 267.
Alissandrakis, C.E., Gel'Frejkh, G.B., Borovik, V.N., Korzhavin, A.N., Bogod, V.M., Nindos, A., Kundu, M.R.: 1993, *Astron. Astrophys.* **270**, 509.
Aschwanden, M.J., Bastian, T.S.: 1994, *Astrophys. J.* **426**, 434.
Aschwanden, M.J., Lim, J., Gary, D.E., Klimchuk, J.A.: 1995, *Astrophys. J.* **454**, 512.
Aubier, M., Leblanc, Y., Boischot, A.: 1971, *Astron. Astrophys.* **12**, 435.
Avrett, E.H.: 1995, In: Kuhn, J., Penn, M. (eds.) *Infrared Tools for Solar Astrophysics: What's Next? Proc. 15th NSO Sac Peak Workshop*, 303.
Avrett, E.H., Loeser, R.: 2008, *Astrophys. J. Suppl.* **175**, 229.
Bastian, T.S.: 1994, *Astrophys. J.* **426**, 774.
Bastian, T.S., Dulk, G.A., Leblanc, Y.: 1996, *Astrophys. J.* **473**, 539.
Beckers, J.M.: 1972, *Ann. Rev. Astron. Astrophys.* **10**, 73.
Belkora, L., Hurford, G.J., Gary, D.E., Woody, D.P.: 1992, *Astrophys. J.* **400**, 692.
Benz, A.O., Krucker, S., Acton, L.W., Bastian, T.S.: 1997, *Astron. Astrophys.* **320**, 993.
Benz, A.O., Krucker, S.: 1999, *Astron. Astrophys.* **341**, 286.
Benz, A.O., Monstein, C., Meyer, H., Manoharan, P.K., Ramesh, R., Altyntsev, A., Lara, A., Paez, J., Cho, K.-S.: 2009, *Earth Moon Planets* **104**, 277.
Bogod, V.M., Korolkov, D.V.: 1975, *Pisma Astron. Zh.* **1**, 25 (*Soviet Astron. Lett.* **1**, 205).
Borovik, V.N., Gelfreikh, G.B., Lubyshev, B.I.: 1975, *Astron. Zh.* **52**, 97 (*Soviet Astron.* **19**, 57).
Borovik, V.N., Kurbanov, M.S., Livshits, M.A., Ryabov, B.I.: 1990, *Astron. Zh.* **67**, 1038 (*Soviet Astron.* **34**, 522).
Borovik, V.N., Medar, V.G., Korzhavin, A.N.: 1999, *Astron. Lett.* **25**, 250.
Borovik, V.N., Medar, V.G.: 1999, In: Vial, J.-C., Kaldeich-Schümann, B. (eds.) *Plasma Dynamics and Diagnostics in the Solar Transition Region and Corona, 8th SOHO Workshop*, *ESA* **SP-446**, 185.
Brajša, R., Benz, A.O., Temmer, M., Jurdana-Šepić, R., Šaina, B., Wöhl, H.: 2007, *Solar Phys.* **245**, 167.
Brajša, R., Romštajn, I., Wöhl, H., Benz, A.O., Temmer, M., Roša, D.: 2009, *Astron. Astrophys.* **493**, 613.
Brajša, R., Ruždjak, V., Vršnak, B., Wöhl, H., Pohjolainen, S., Upro, S.: 2000, *Solar Phys.* **196**, 279.
Briand, C., Zaslavsky, A., Maksimovic, M., Zarka, P., Lecacheux, A., Rucker, H.O., Konovalenko, A.A., Abranin, E.P., Dorovsky, V.V., Stanislavsky, A.A., Melnik, V.N.: 2008, *Astron. Astrophys.* **490**, 339.
Brosius, J.W., White, S.M.: 2006, *Astrophys. J.* **641**, L69.
Carlsson, M., Stein, R.F.: 2002, *Astrophys. J.* **572**, 626.
Chiuderi, C., Chiuderi Drago, F.: 2004, *Astron. Astrophys.* **422**, 331.
Chiuderi Drago, F.: 1990, In: Ruzdjak, V., Tandberg-Hanssen, E. (eds.) *Dynamics of Quiescent Prominences, Proc. of the No. 117 Colloquium of the IAU*, *Lecture Notes in Physics* **363**, 70.
Chiuderi Drago, F., Kundu, M.R., Schmahl, E.J.: 1983, *Solar Phys.* **85**, 237.
Chiuderi Drago, F., Alissandrakis, C.E., Bastian, T., Bocchialini, K., Harrison, R.A.: 2001, *Solar Phys.* **199**, 115.
Chiuderi Drago, F., Landi, E., Fludra, A., Kerdraon, A.: 1999, *Astron. Astrophys.* **348**, 261.
Cohen, M.H.: 1960, *Astrophys. J.* **131**, 664.
Crosby, N., Vilmer, N., Chiuderi Drago, F., Pick, M., Kerdraon, A., Khan, J., Schwenn, R.: 1997, In: Wilson, A. (ed.) *Fifth SOHO Workshop: The Corona and Solar Wind Near Minimum Activity*, *ESA SP-404*, 299.
Dudík, J., Kulinová, A., Dzifčáková, E., Karlický, M.: 2009, *Astron. Astrophys.* **505**, 1255.

Dulk, G.A., Sheridan, K.V.: 1974, *Solar Phys.* **36**, 191.
Efanov, V.A., Moiseev, I.G., Nesterov, N.S., Stewart, R.T.: 1980, In: Kundu, M.R., Gergely, T.E. (eds.) *Radio Physics of the Sun*, Reidel, Dordrecht, 141.
Erskine, F.T., Kundu, M.R.: 1982, *Solar Phys.* **76**, 221.
Fontenla, J.M., Avrett, E.H., Loeser, R.: 1990, *Astrophys. J.* **355**, 700.
Fontenla, J.M., Avrett, E.H., Loeser, R.: 1991, *Astrophys. J.* **377**, 712.
Fontenla, J.M., Avrett, E.H., Loeser, R.: 1993, *Astrophys. J.* **406**, 319.
Fontenla, J.M., Avrett, E.H., Loeser, R.: 2002, *Astrophys. J.* **572**, 636.
Fontenla, J.M., Avrett, E., Thuillier, G., Harder, J.: 2006, *Astrophys. J.* **639**, 441.
Fontenla, J.M., Balasubramaniam, K.S., Harder, J.: 2007, *Astrophys. J.* **667**, 1243.
Fontenla, J.M., Curdt, W., Haberreiter, M., Harder, J., Tian, H.: 2009, *Astrophys. J.* **707**, 482.
Gary, D.E.: 1996, In: Taylor, A.R., Paredes, J.M. (eds.) *Radio Emission from the Stars and the Sun*, *ASP Conf. Series* **93**, 387.
Gary, D.E., Hartl, M.D., Shimizu, T.: 1997, *Astrophys. J.* **477**, 958.
Gary, D.E., Zirin, H.: 1988, *Astrophys. J.* **329**, 991.
Gary, D.E., Zirin, H., Wang, H.: 1990, *Astrophys. J.* **355**, 321.
Gelfreikh, G.B.: 1998, In: Alissandrakis, C.E., Schmieder, B. (eds.) *Three-Dimensional Structure of Solar Active Regions, 2nd Advances in Solar Physics Euroconference*, *ASP Conf. Series* **155**, 110.
Gelfreikh, G.B., Kaidanovskii, M.N., Kononovich, E.V., Smirnova, O.B., Stotskii, A.A., Trushkin, S.A.: 1977, *Pisma Astron. Zh.* **3**, 550 (*Soviet Astron. Lett.* **3**, 300).
Gelfreikh, G.B., Grechnev, V., Kosugi, T., Shibasaki, K.: 1999, *Solar Phys.* **185**, 177.
Gelfreikh, G.B., Lubyshev, B.I.: 1979, *Astron. Zh.* **56**, 562 (*Soviet Astron.* **23**, 316).
Gingerich, O., de Jager, C.: 1968, *Solar Phys.* **3**, 5.
Gingerich, O., Noyes, R.W., Kalkofen, W., Cuny, Y.: 1971, *Solar Phys.* **18**, 347.
Gopalswamy, N., Shibasaki, K., Thompson, B.J., Gurman, J., DeForest, C.: 1999, *J. Geophys. Res.* **104**, 9767.
Grebinskij, A., Bogod, V., Gelfreikh, G., Urpo, S., Pohjolainen, S., Shibasaki, K.: 2000, *Astron. Astrophys. Suppl. Ser.* **144**, 169.
Grechnev, V.V., Lesovoi, S.V., Smolkov, G.Y., Krissinel, B.B., Zandanov, V.G., Altyntsev, A.T., Kardapolova, N.N., Sergeev, R.Y., Uralov, A.M., Maksimov, V.P., Lubyshev, B.I.: 2003, *Solar Phys.* **216**, 239.
Heintze, J.R.W., Hubenet, H., de Jager, C.: 1964, *SAO Spec. Rep.* **167**, 240.
Hoang, S., Steinberg, J.L.: 1977, *Astron. Astrophys.* **58**, 287.
Irimajiri, Y., Takano, T., Nakajima, H., Shibasaki, K., Hanaoka, Y., Ichimoto, K.: 1995, *Solar Phys.* **156**, 363.
Kakinuma, T., Swarup, G.: 1962, *Astrophys. J.* **136**, 975.
Karlický, M., Bárta, M., Dąbrowski, B.P., Heinzel, P.: 2011, *Solar Phys.* **268**, 165.
Kaufmann, P., Levato, H., Cassiano, M.M., Correia, E., Costa, J.E.R., Giménez de Castro, C.G., Godoy, R., Kingsley, R.K., Kingsley, J.S., Kudaka, A.S., Marcon, R., Martin, R., Marun, A., Melo, A.M., Pereyra, P., Raulin, J.-P., Rose, T., Valio, A. Silva, Walber, A., Wallace, P., Yakubovich, A., Zakia, M.B.: 2008, In: *Society of Photo-Optical Instrumentation Engineers (SPIE) Conference Series* **7012**, 70120L.
Keller, C.U., Krucker, S.: 2004, In: Gary, D.E., Keller, C.U. (eds.) *Solar and Space Weather Radiophysics*, Kluwer Academic, Dordrecht, 287.
Kerdraon, A., Delouis, J.-M.: 1997, In: Trottet, G. (ed.) *Coronal Physics from Radio and Space Observations*, *Lecture Notes in Physics* **483**, 192.
Kosugi, T., Ishiguro, M., Shibasaki, K.: 1986, *Publ. Astron. Soc. Japan* **38**, 1.
Krissinel, B.B.: 2005, *Astron. Rep.* **49**, 939.
Krissinel, B.B., Kuznetsova, S.M., Maksimov, V.P., Prosovetsky, D.V., Grechnev, V.V., Stepanov, A.P., Shishko, L.F.: 2000, *Publ. Astron. Soc. Japan* **52**, 909.
Krucker, S., Benz, A.O.: 2000, *Solar Phys.* **191**, 341.
Krucker, S., Benz, A.O., Bastian, T.S., Acton, L.W.: 1997, *Astrophys. J.* **488**, 499.
Kundu, M.R.: 1965, *Solar Radio Astronomy*, Interscience, New York.
Kundu, M.R., Alissandrakis, C.E.: 1975a, *Nature* **257**, 465.
Kundu, M.R., Alissandrakis, C.E.: 1975b, *Mon. Not. Roy. Astron. Soc.* **173**, 65.
Kundu, M.R., Rao, A.P., Erskine, F.T., Bregman, J.D.: 1979, *Astrophys. J.* **234**, 1122.
Kundu, M.R., Velusamy, T.: 1974, *Solar Phys.* **34**, 125.
Landi, E., Chiuderi Drago, F.: 2003, *Astrophys. J.* **589**, 1054.
Landi, E., Chiuderi Drago, F.: 2008, *Astrophys. J.* **675**, 1629.
Lantos, P., Kundu, M.R.: 1972, *Astron. Astrophys.* **21**, 119.
Lantos, P.: 1999, In: Bastian, T., Gopalswamy, N., Shibasaki, K. (eds.) *Solar Physics with Radio Observations*, *NRO Report* **479**, 11.
Lantos, P., Alissandrakis, C.E.: 1999, *Astron. Astrophys.* **351**, 373.
Lantos, P., Alissandrakis, C.E., Gergely, T., Kundu, M.R.: 1987, *Solar Phys.* **112**, 325.

Lantos, P., Alissandrakis, C.E., Rigaud, D.: 1992, *Solar Phys.* **137**, 225.
Lee, J.: 2007, *Space Sci. Rev.* **133**, 73.
Lee, J., McClymont, A.N., Mikic, Z., White, S.M., Kundu, M.R.: 1998, *Astrophys. J.* **501**, 853.
Loukitcheva, M., Solanki, S.K., Carlsson, M., Stein, R.F.: 2004, *Astron. Astrophys.* **419**, 747.
Loukitcheva, M., Solanki, S.K., White, S.: 2006, *Astron. Astrophys.* **456**, 713.
Loukitcheva, M., Solanki, S.K., White, S.M.: 2009, *Astron. Astrophys.* **497**, 273.
Loukitcheva, M., Solanki, S.K., White, S.M.: 2010, *Mem. Soc. Astron. Ital.* **81**, 592.
Lubyshev, B.I.: 1977, *Astron. Zh.* **54**, 130 (*Soviet Astron.* **21**, 74).
Marqué, C.: 2004, *Astrophys. J.* **602**, 1037.
Marqué, C., Lantos, P., Delouis, J.M., Alissandrakis, C.E.: 1999, In: Vial, J.-C., Kaldeich-Schümann, B. (eds.) *Plasma Dynamics and Diagnostics in the Solar Transition Region and Corona, 8th SOHO Workshop*, *ESA* **SP-446**, 483.
McConnell, D.: 1982, *Solar Phys.* **78**, 253.
Mercier, C., Chambe, G.: 2009, *Astrophys. J. Lett.* **700**, L137.
Mercier, C., Subramanian, P., Kerdraon, A., Pick, M., Ananthakrishnan, S., Janardhan, P.: 2006, *Astron. Astrophys.* **447**, 1189.
Moran, T., Gopalswamy, N., Dammasch, I.E., Wilhelm, K.: 2001, *Astron. Astrophys.* **378**, 1037.
Nakajima, H., Nishio, M., Enome, S., Shibasaki, K., Takano, T., Hanaoka, Y., Torii, C., Sekiguchi, H., Bushimata, T., Kawashima, S., Shinohara, N., Irimajiri, Y., Koshiishi, H., Kosugi, T., Shiomi, Y., Sawa, M., Kai, K.: 1994, *Proc. IEEE* **82**, 705.
Nindos, A., Alissandrakis, C.E., Gelfreikh, G.B., Borovik, V.N., Korzhavin, A.N., Bogod, V.M.: 1996, *Solar Phys.* **165**, 41.
Nindos, A., Aurass, H.: 2007, In: Klein, K.-L., MacKinnon, A.L. (eds.) *The High Energy Solar Corona: Waves, Eruptions, Particles*, *Lecture Notes in Physics* **725**, 251.
Nindos, A., Kundu, M.R., White, S.M.: 1999, *Astrophys. J.* **513**, 983.
Nindos, A., Kundu, M.R., White, S.M., Gary, D.E., Shibasaki, K., Dere, K.P.: 1999, *Astrophys. J.* **527**, 415.
Nindos, A., Kundu, M.R., White, S.M., Shibasaki, K., Gopalswamy, N.: 2000, *Astrophys. J. Suppl.* **130**, 485.
Noyes, R.W., Beckers, J.M., Low, F.J.: 1968, *Solar Phys.* **3**, 36.
Oberoi, D., Matthews, L.D., Cairns, I.H., Emrich, D., Lobzin, V., Lonsdale, C.J., Morgan, E.H., Prabu, T., Vedantham, H., Wayth, R.B., Williams, A., Williams, C., White, S.M., *et al.*: 2011, *Astrophys. J. Lett.* **728**, L27.
Pohjolainen, S.: 2000, *Astron. Astrophys.* **361**, 349.
Pohjolainen, S., Portier-Fozzani, F., Ragaigne, D.: 2000, *Astron. Astrophys. Suppl. Ser.* **143**, 227.
Ramesh, R., Kathiravan, C., Barve, I.V., Beeharry, G.K., Rajasekara, G.N.: 2010, *Astrophys. J. Lett.* **719**, L41.
Ramesh, R., Kathiravan, C., Sastry, C.V.: 2010, *Astrophys. J.* **711**, 1029.
Riehokainen, A., Urpo, S., Valtaoja, E., Makarov, V.I., Makarova, L.V., Tlatov, A.G.: 2001, *Astron. Astrophys.* **366**, 676.
Riehokainen, A., Valtaoja, E., Pohjolainen, S.: 2003, *Astron. Astrophys.* **402**, 1103.
Rosa, D., Vrsnak, B., Bozic, H., Brajsa, R., Ruzdjak, V., Schroll, A., Wohl, H.: 1998, *Solar Phys.* **179**, 237.
Ryabov, B.I., Pilyeva, N.A., Alissandrakis, C.E., Shibasaki, K., Bogod, V.M., Garaimov, V.I., Gelfreikh, G.B.: 1999, *Solar Phys.* **185**, 157.
Selhorst, C.L., Silva, A.V.R., Costa, J.E.R.: 2004, *Astron. Astrophys.* **420**, 1117.
Selhorst, C.L., Silva, A.V.R., Costa, J.E.R.: 2005, *Astron. Astrophys.* **433**, 365.
Selhorst, C.L., Silva-Válio, A., Costa, J.E.R.: 2008, *Astron. Astrophys.* **488**, 1079.
Selhorst, C.L., Giménez de Castro, C.G., Varela Saraiva, A.C., Costa, J.E.R.: 2010, *Astron. Astrophys.* **509**, A51.
Shibasaki, K.: 1998, In: Balasubramaniam, K.S., Harvey, J., Rabin, D. (eds.) *Synoptic Solar Physics*, *ASP Conference Series* **140**, 373.
Shibasaki, K.: 1999, In: Bastian, T., Gopalswamy, N., Shibasaki, K. (eds.) *Solar Physics with Radio Observations*, *NRO Report* **479**, 1.
Shibasaki, K., Enome, S., Nakajima, H., Nishio, M., Takano, T., Hanaoka, Y., Torii, C., Sekiguchi, H., Kawashima, S., Bushimata, T., Shinohara, N., Koshiishi, H., Shiomi, Y., Irimajiri, Y., Leka, K.D., Canfield, R.C.: 1994, *Publ. Astron. Soc. Japan* **46**, L17.
Silva, A.V.R., Laganá, T.F., Castro, C.G. Gimenez, Kaufmann, P., Costa, J.E.R., Levato, H., Rovira, M.: 2005, *Solar Phys.* **227**, 265.
Sych, R.A., Nakariakov, V.M., Anfinogentov, S.A., Ofman, L.: 2010, *Solar Phys.* **266**, 349.
Tanaka, H., Castelli, J.P., Covington, A.E., Krüger, A., Landecker, T.L., Tlamicha, A.: 1973, *Solar Phys.* **29**, 243.
Tapping, K.F., Boteler, D., Charbonneau, P., Crouch, A., Manson, A., Paquette, H.: 2007, *Solar Phys.* **246**, 309.

Thejappa, G., Kundu, M.R.: 1992, *Solar Phys.* **140**, 19.
Thejappa, G., Kundu, M.R.: 1994, *Solar Phys.* **149**, 31.
Thejappa, G., MacDowall, R.J.: 2008, *Astrophys. J.* **676**, 1338.
Tun, S.D., Gary, D.E., Georgoulis, M.K.: 2011, *Astrophys. J.* **728**, 1.
Vernazza, J.E., Avrett, E.H., Loeser, R.: 1973, *Astrophys. J.* **184**, 605.
Vernazza, J.E., Avrett, E.H., Loeser, R.: 1976, *Astrophys. J. Suppl.* **30**, 1.
Vernazza, J.E., Avrett, E.H., Loeser, R.: 1981, *Astrophys. J. Suppl.* **45**, 635.
Vocks, C., Mann, G.: 2004, *Astron. Astrophys.* **419**, 763.
Vourlidas, A., Gary, D.E., Shibasaki, K.: 2006, *Publ. Astron. Soc. Japan* **58**, 11.
White, S.M.: 2004, In: Gary, D.E., Keller, C.U. (eds.) *Solar and Space Weather Radiophysics*, Kluwer Academic, Dordrecht, 89.
White, S.M., Kundu, M.R., Shimizu, T., Shibasaki, K., Enome, S.: 1995, *Astrophys. J.* **450**, 435.
White, S.M., Loukitcheva, M., Solanki, S.K.: 2006, *Astron. Astrophys.* **456**, 697.
Zhang, J., Kundu, M.R., White, S.M., Dere, K.P., Newmark, J.S.: 2001, *Astrophys. J.* **561**, 396.
Zheleznyakov, V.V.: 1962, *Astron. Zh.* **39**, 5 (*Soviet Astron.* **6**, 3).
Zheleznyakov, V.V.: 1970, *Radio Emission of the Sun and Planets*, Pergamon Press, Oxford.
Zirin, H., Baumert, B.M., Hurford, G.J.: 1991, *Astrophys. J.* **370**, 779.